Analysis of Diesel Spray Dynamics Using a Compressible Eulerian/VOF/LES Model and Microscopic Shadowgraphy

M. Ghiji[*, 1], L. Goldsworthy[1], P.A. Brandner[1], V. Garaniya[1], and P. Hield[2]

[1]*Australian Maritime College, University of Tasmania, Tasmania, Australia*

[2]*Defence Science and Technology Group, Victoria, Australia*

Abstract

This paper presents numerical and experimental analysis of diesel engine spray dynamics in the region very close to the nozzle exit. Diesel fuel is injected through a single solid cone injector with sharp-edged nozzle inlet. Numerical investigations are conducted in an Eulerian framework by applying a Volume of Fluid interface capturing technique integrated with Large-Eddy Simulation turbulence modelling. Cavitation is modelled, by allowing liquid fuel to flash to gas at the fuel vapour pressure. The computational domain and settings mimic the experimental injector internal geometry and experimental operating conditions. In-nozzle disturbances are qualitatively well modelled by implementing the no-slip condition at the injector walls as well as cavitation and compressibility effects for each phase. A mesh dependency study is conducted with four different grid resolutions. Data are presented around the start of penetration (SOP) and up to the time when shock waves at the gas-liquid interface are well developed, the quasi-steady stage of injection. At SOP, an umbrella-shaped leading edge is captured in both the numerical and experimental studies however only the experimental images demonstrated a semi-transparent cloud of air-fuel mixture at the leading edge. A previously undescribed toroidal starting vortex near the nozzle exit is captured experimentally and numerically. Development of cavitation, down to the end of nozzle hole leads to the detachment of liquid from the nozzle hole walls and subsequently the diminution of boundary layer effects and thus reduced in-nozzle turbulence, and increased liquid jet velocity.

Keywords: Primary atomization; Diesel spray; Large Eddy Simulation; Cavitation; Shock wave; Compressible flow

*Corresponding author.
Email address: mghiji@utas.edu.au (M. Ghiji)

1 Introduction

Engine emissions are produced during the combustion process which is fundamentally controlled by the dynamics of the fuel injection [1-6]. There is a wide range of fuel injectors based on their shapes and flow characteristics but the purpose of most injectors is still the same, to induce atomization, penetration, turbulence generation and gas-fuel mixing. Undoubtedly, a clear understanding of these processes would assist engineers to design an injector which not only meets strict pollution requirements but also improve engine performance in one of the most extreme environments for multiphase flow. In this harsh environment, shock waves [7] and turbulent eddies [8] are expected, which makes understanding of the spray dynamics a challenge for designers and scientists.

The atomization process which initiates very close to the nozzle hole exit, is called primary atomization and controls the extension of the liquid core and subsequently the secondary atomization in the disperse flow region [9, 10]. To date, many theories have been proposed to describe the primary atomization mechanism, including: Aerodynamic shear forces which act through stripping and Kelvin-Helmholtz (K-H) instabilities [11-13]; Turbulence-induced disintegration which has a significant effect on jet breakup in higher Reynolds number $Re_l = \rho_l V D / \mu_l$, where ρ_l is the liquid density, V is the liquid velocity, D is the orifice diameter, and μ_l is the liquid dynamic viscosity [14-17]; Relaxation of the velocity profile, creating a "bursting" effect especially in non-cavitating jets and large velocity differentials [18]; Cavitation-induced disintegration of the jet due to the reduction of cross-section area at nozzle inlet [19-22]; and liquid bulk oscillation provoking the toroidal surface perturbation [12, 23].

For nozzles with small length-to-diameter ratios super-cavitation and hydraulic flip can occur [24]. In these cases, the liquid fuel which has detached at the nozzle inlet remains detached from the walls throughout the entire nozzle passage, and the liquid core is contracted at the nozzle exit compared to the nozzle size, so the mass flow rate is reduced. If the length of the nozzle passage is long enough, or if the injection pressure is not high, the liquid flow can re-attach to the walls downstream of the nozzle hole inlet [25, 26]. In this case, the discharge coefficient is higher compared to that of the super-cavitation case.

Based on the Reynolds and Ohnesorge numbers of the flow, the breakup of liquid jets is categorized into four regimes; Rayleigh breakup, first wind-induced breakup, second wind-induced breakup, and atomization [27]. These parameters also change with different fuels. Detailed studies comparing different fuels and the influence on spray structure and formation have been made by Payri et.al [28, 29], Desantes et.al [30], Battistoni et.al [31], and Goldsworthy et.al [32]. For diesel propulsion systems, the liquid propellants fall well within the atomization regime. In such regime, average drop diameters are much less than the jet diameter, thus indicating that the scale in which flow instabilities arise is much smaller than the jet diameter. Furthermore, liquid jets within this regime experience stronger axial velocity gradients in the near exit region than the jets in other regimes due to faster relaxation of the liquid surface as it transitions from a no-slip boundary (except in the case of “super-cavitation”) to a free surface boundary condition as it exits the injector nozzle.

The existence of shock waves in high pressure diesel spray was first reported by Nakahira et al. [33] and most recently by Huang et al. [7] using the schlieren image technique. Hillamo et al [34] demonstrated the imaging of shock waves from a diesel spray using the backlit imaging technique. An increase of 15% in the gaseous phase density near the shock front was quantitatively demonstrated by MacPhee et al. [35] using the X-ray radiograph image technique.

In experimentations, isolating and quantifying the various interactive mechanisms involved in primary atomization of a high-pressure liquid jet are very difficult [13, 36-40]. Hence, numerical analysis can be employed to get a clearer insight into the effect of each parameter at different stages of the injection process [4, 41].

Generated turbulent flows can be represented by eddies with a range of length and time scales. Large eddy simulation (LES) directly resolves large scale eddies and models small eddies, allowing the use of much coarser meshes and longer time steps in LES compared to Direct Numerical Simulation (DNS). LES needs principally finer meshes compared to the ones used for Reynolds Averaged Navier-Stokes (RANS) computations. Since RANS models cannot capture features of the transient spray structure [9, 12, 42, 43] such as droplet clustering and shot to shot variability, LES is applied to overcome these limitations. In addition, the conventional atomization models with Lagrangian Particle Tracking (LPT) limit the grid fineness near the nozzle and do not allow LES to capture the features of the spray and background fluid flow near the nozzle. Refining the grid with the blob atomization method can result in problems with a high liquid fraction in the LPT approach (too much liquid in each cell) [9, 42-44]. These limitations motivate the use of the Eulerian approach to model the primary atomization, instead of using LPT atomization models. With ever increasing computational power there is an incentive to use more complex models for primary atomization.

The accuracy of different numerical techniques for modelling the primary atomization of a liquid diesel jet was investigated in detail for low *Re* ($Re < 5000$) by Herrmann [14] and Desjardins & Pitsch [45]. Herrman [14] demonstrated the importance of the grid resolution on capturing the accurate phase interface geometry of diesel liquid with an injection velocity of 100 m/s and $Re = 5000$. Turbulence was reported as the dominant driving mechanism of atomization within the first 20 nozzle diameters downstream.

The present study focuses on experimental and numerical investigation of the primary atomization in the early stages of injection with increasing injection pressure up to 1200 bar, background pressure of 30 bar, liquid Re of $7\times10^3 \leq Re_l \leq 46\times10^3$, and liquid Weber number of $4\times10^4 \leq We_l \leq 2\times10^6$. The liquid Weber number (We_l) is defined as $\rho_l\, V\, D\, /\, \sigma$, where σ is the surface tension at the liquid-gas interface. Recent work using X-ray imaging [46-48], especially from the Argonne Laboratory has greatly enhanced our understanding of diesel spray dynamics. The experimental techniques presented here, while less sophisticated are more accessible and give useful data on the spray morphology for comparison with numerical analysis.

A key aim of the present work is to achieve a valid (high-fidelity) Computational Fluid Dynamics (CFD) modelling of diesel spray primary atomization which can be applied by engine developers for improved design of diesel engines. A further aim is to apply the numerical and experimental analysis to enhance understanding of in- and near-nozzle processes.

2 Methodology

Experimental measurements are used to validate the numerical results at various stages of the injection event. The experiments employed a microscopic laser-based backlight imaging (shadowgraphy) technique using a constant volume spray chamber.

Numerical investigations are conducted by applying the VOF phase-fraction interface capturing technique in an Eulerian LES framework where cavitation of the fuel is allowed at a predefined vapor pressure. Enhanced cavitation inception due to nuclei is not modelled. The effects of compressibility of each phase have been included in the numerical model, enabling the investigation of more complex physics associated with a diesel spray process such as viscosity and temperature changes, generation and development of cavitation and gaseous shock waves.

2.1 Experimental Set-up

The experimental apparatus consists of a constant volume High-Pressure Spray Chamber (HPSC). The HPSC operating volume is a square-section prism with rounded corners, with the chamber and spray axes vertically oriented. Optical access to the chamber is via three windows of UV quality, optically polished quartz, with viewing area of 200 × 70 mm. The chamber pressure can be varied to emulate the air density occurring in a diesel engine at the start of injection. Diesel fuel is injected axially through a single solid cone fuel spray with an adjustable injection pressure up to 1200 bar from the top of HPSC as shown in Figure 1. A continuous flow of air through the chamber removes droplets from previous shots. Tests were made to ensure that any turbulence induced by the flushing air did not impact on the spray dynamics, by closing off the flushing air flow and observing if this impacted on the spray morphology.

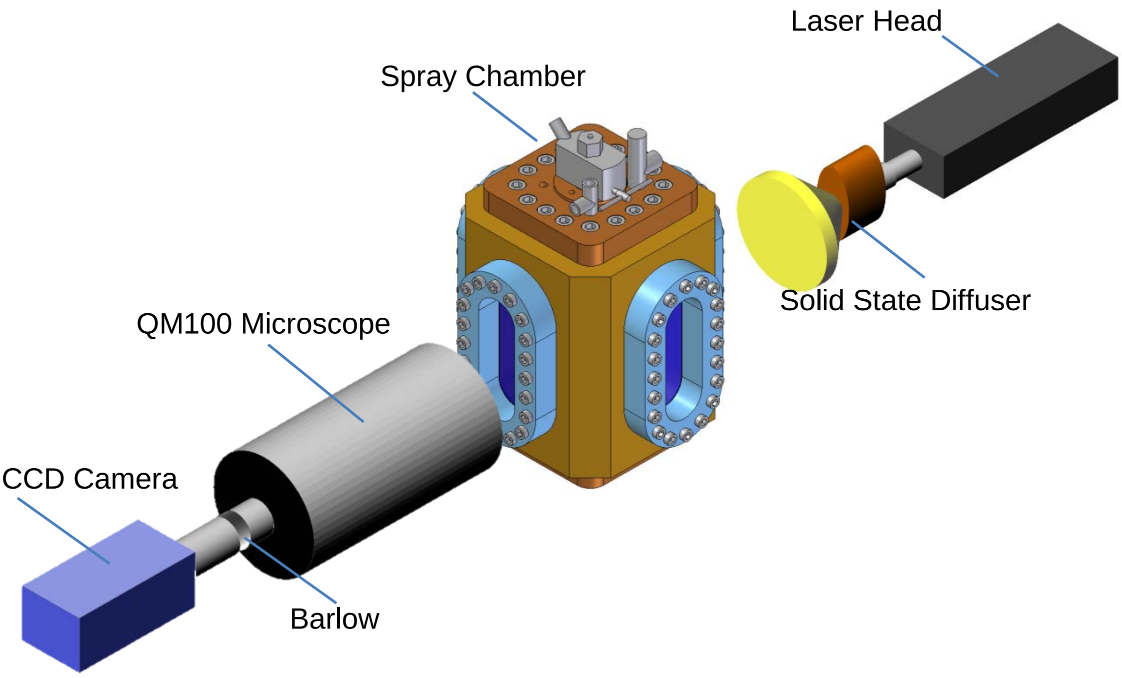

Figure 1. The experimental apparatus for shadowgraphy measurements.

The injection pressure profile is highly repeatable from shot to shot. The injector needle valve snaps open when the injector pressure achieves a certain value, as determined by the adjustable tension on the needle valve spring. The needle lift is monitored using an eddy current proximity probe. The needle lift transducer indicates that it takes about 200 µs for the needle valve to lift completely. The maximum needle lift is nominally 200 µm. The needle lift commences around 100 µs after the start of injection. However, the response of this transducer may not exactly indicate the motion of the needle as the needle lift detector is mounted on the spring actuating rod rather than the needle itself, so compression of the actuating rod could mask the actual needle motion, and there is potentially some lag in the electronics.

A Kistler piezoelectric pressure transducer with a sample rate of 10 MHz monitors the pressure of the fuel supplied to the injector. The high-pressure fuel pulse is generated in a modified Hydraulic Electric Unit Injector (HEUI) as described in Goldsworthy et al. [32, 49]. The ability to independently adjust the needle lift pressure allows relatively high pressures at the point of needle lift, which is more characteristic of common rail injectors than of conventional injectors.

The spray is illuminated with laser light through a standard solid state diffuser supplied by LaVision. The diffuser employs laser-induced fluorescent from an opaque plate impregnated with a fluorescent dye. A 120 mJ dual-cavity Nd:YAG laser is used and in combination with the solid state diffuser, light pulses of duration around 10 ns are achieved. A Questar QM100 long distance microscope is attached to a LaVision Imager Intense dual-frame, 12 bit CCD camera with 1376 × 1040 pixel resolution. The camera is focused, aligned, and calibrated on a graduated scale on the spray axis. With a 2x Barlow lens, mounted between CCD Camera and Microscope, a magnification of 7.7:1, a field of view of 1157 × 860 μm and a spatial resolution of 0.84 μm/pixel are achieved.

Data acquisition is initiated at a pre-set threshold of fuel pressure, with an adjustable delay to the acquisition of the images. The camera and laser allow two images with variable time gap as low as 1 μs to be taken for each shot of the injector. The Qswitch signal from the laser indicating that the laser has been fired is acquired in LabVIEW along with the injection pressure and needle lift signal. This indicates the timing of the data acquisition relative to the needle lift and pressure development. The start of penetration is found to be 100±5 μs before the needle lift signal reached 2% of its maximum value. This delay is assumed to be due to compression/buckling of the rod which transmits the spring force to the needle, and electronic delay in the needle lift transducer. The timing jitter of ±5 μs means that meaningful comparison of numerical and experimental penetration against time could not be made with sufficient precision, so instead the consecutive imaging technique is employed. In this technique, to determine the time from SOP to the taking of the second image, shots are repeated until the first image acquired corresponds to the SOP and thus the pre-set delay to the second image represents the time After Start Of Penetration (ASOP). An interval of about 30 seconds between injector shots allows the gas in the chamber settle.

2.2 Numerical Approach

2.2.1 Mathematical Method

In this study, the compressible VOF phase-fraction based interface capturing technique is employed in the open source numerical code OpenFOAM v2.3. The governing equations of the solver which is based on *compressibleInterFoam,* consist of the balances of mass (1), momentum (2), total energy (3), and enthalpy (4) for two immiscible, compressible fluids with the inclusion of the surface tension between two phases and the equation of state (9). These equations establish a closed system for the variables density ρ, velocity $\boldsymbol{V}$, pressure *p*, internal energy $\widehat{U}$, and enthalpy $\hat{h}$,

$$\frac{\partial \rho}{\partial t} + \nabla.(\rho \boldsymbol{V}) = 0 \tag{1}$$

$$\frac{\partial \rho \boldsymbol{V}}{\partial t} + \nabla.\left(\rho \boldsymbol{V} \otimes \boldsymbol{V}\right) = -\nabla p + \nabla.\tau + \rho \boldsymbol{g} + \int_{S(t)} \sigma \boldsymbol{\kappa} \boldsymbol{n} \delta(x - x')dS \tag{2}$$

$$\frac{\partial \rho \widehat{U}}{\partial t} + \nabla.\left(\rho \widehat{\boldsymbol{U}} \boldsymbol{V}\right) + \frac{\partial \rho \boldsymbol{K}}{\partial t} + \nabla.(pK\boldsymbol{V}) + \nabla.(p\boldsymbol{V}) = -\nabla.\mathrm{q} - \nabla.(\tau.\boldsymbol{V}) + \rho \boldsymbol{g}.\boldsymbol{V} \tag{3}$$

$$\frac{\partial \rho \hat{h}}{\partial t} + \nabla.\left(\rho \hat{\boldsymbol{h}} \boldsymbol{V}\right) + \frac{\partial \rho \boldsymbol{K}}{\partial t} + \nabla.(pK\boldsymbol{V}) - \frac{\partial p}{\partial t} = -\nabla.\mathrm{q} - \nabla.(\tau.\boldsymbol{V}) + \rho \boldsymbol{g}.\boldsymbol{V} \tag{4}$$

where, μ is the dynamic viscosity, *t* is the time, $\boldsymbol{g}$ is the gravitational acceleration, σ is the surface tension, *K* is the kinetic energy, q is the thermal energy flux vector, τ is the viscous stress tensor, κ is the local curvature of the liquid surface and, *n* denotes a unit vector normal to the liquid surface *S*. The operators $\nabla(\ )$ and $\nabla.(\ )$ represent the gradient and the divergence operations, respectively.

The momentum source due to surface tension force on the interface *S(t)*, the integral term in equation (2), only acts on *S* and produces a non-zero value when $x = x'$ which is an indication of the existence of an interface. The estimation of this integral term is obtained following De Villier [50] through the continuum surface force model of Brackbill et al. [51] as:

$$\int_{S(t)} \sigma \boldsymbol{\kappa} \boldsymbol{n} \delta(x - x')dS \approx \sigma \boldsymbol{\kappa} \nabla . \gamma \tag{5}$$

where γ is the volume fraction of the liquid phase defined as:

$$\gamma = \begin{cases} 1 & \text{for a point inside the liquid} \\ 0 < \gamma < 1 & \text{for a point in the transitional region} \\ 0 & \text{for a point inside the gas} \end{cases} \tag{6}$$

The 'transitional region' is where the interface is located, realized as an artefact of the numerical solution process. Fluid in the transition region is considered as a mixture of the two fluids on each side of the interface, which cannot completely resolve a discontinuous step. The volume fraction is obtained from the solution of a transport equation:

$$\frac{\partial \rho \gamma}{\partial t} + \nabla . (\rho \boldsymbol{V} \gamma) = 0 \tag{7}$$

The interface curvature, κ, calculated from the solution of liquid phase volume fraction γ is

$$\boldsymbol{\kappa} = \nabla . \left(\frac{\nabla \gamma}{|\nabla \gamma|} \right) \tag{8}$$

The system of equations are closed by an equation of state

$$\begin{cases} \rho_l = p\, \psi_l \\ \rho_g = p\, \psi_g \end{cases} \tag{9}$$

where ψ is the compressibility and the subscripts l and g represent the liquid and gas phases respectively.

The local thermo-physical properties are given by:

$$\rho = \gamma \rho_l + (1 - \gamma)\rho_g \tag{10}$$

$$\mu = \gamma \mu_l + (1 - \gamma)\mu_g \tag{11}$$

The time-varying phase interface *S(t)* is located using a VOF surface capturing/tracking approach [52] which utilizes a "compression velocity" term [53] in equation (7) to preserve sharp interfaces.

The LES/VOF equations are derived from equations (2), (1) and (7) using localized volume averaging of the phase-weighted hydrodynamics variables. This process, known as filtering, includes decomposition of the relevant variables into resolvable and sub-grid scales of turbulent fluctuations. As a result of the filtering process, the sub-grid scale fluctuations will be eliminated from the direct simulation. This filtering together with the non-linear convection terms in equation (2) introduce an additional quantity which is known as the sub-grid scale (SGS) stresses τ^{sgs}. The SGS stresses comprise correlation of the variable fluctuations at sub-grid scales that entail closure through mathematical models, given by:

$$\tau^{sgs} = \overline{\boldsymbol{V}\boldsymbol{V}} - \overline{\boldsymbol{V}}\overline{\boldsymbol{V}} \tag{12}$$

and estimated by a sub-grid scale model of the eddy-viscosity type:

$$\tau^{sgs} - \frac{2}{3}\, k\, \boldsymbol{I} = -\frac{\mu^{sgs}}{\rho}\, (\nabla\overline{\boldsymbol{V}} + \nabla\overline{\boldsymbol{V}}^{T}) \tag{13}$$

where I is the identity tensor, k is the sub-grid scale turbulent energy and μ^{sgs} is the sub-grid scale viscosity. Both are determined from the one-equation SGS turbulent energy transport model accredited to Yoshizawa [54]:

$$\frac{\partial k}{\partial t} + \nabla.(k\overline{\boldsymbol{V}}) = \nabla.[(\vartheta + \vartheta^{sgs})\nabla k + \tau^{sgs}\cdot\overline{\boldsymbol{V}}] - \varepsilon - \frac{1}{2}\tau^{sgs} : (\nabla\overline{\boldsymbol{V}} + \nabla\overline{\boldsymbol{V}}^{T}) \tag{14}$$

where $\varepsilon = C_\varepsilon\, \rho\, k^{(3/2)}/\Delta$ is the SGS turbulent dissipation $\vartheta^{sgs} = C_k\, \rho\, k^{(1/2)}/\Delta$ is the SGS kinematic viscosity and $\Delta = V^{(1/3)}$ is the SGS length scale where V is the volume of the computational cell. The coefficients, found from statistical considerations, are $C_\varepsilon = 1$ and $C_k = 0.05$ [9].

The gaseous phase is represented by air. Any fuel vapor produced by low-pressure evaporation is given the properties of air. Fuel is allowed to vaporize when its pressure falls to the vapor pressure of diesel fuel at ambient temperature 1 kPa [26]. This flash boiling model can be considered as a basic cavitation model. Specific heat capacity, dynamic viscosity and Prandtl number are constant for each phase.

2.2.2 Numerical Solution Method

Mathematical models are solved by an implicit finite-volume method, which utilizes second order spatial and temporal discretization schemes. The solution procedure employs Pressure Implicit with

Split Operator (PISO) algorithm [55], together with conjugate gradient methods for coupled solution of mass and momentum conservation equations which is specifically suited to transient flows [56]. The advection terms are solved by a bounded Normalized Variable (NV) Gamma differencing scheme [57] with a blending factor of 0.2 and the interface compression scheme (CICSAM) by Ubbink [52] for capturing sharp immiscible interfaces. A conservative, bounded, second order scheme, Gauss linear, is used for Laplacian derivative terms with an additional explicit corrector for mesh non-orthogonality [57]. A second order, implicit discretization scheme (backward) is used for the time derivative terms. The numerical integration time-step is adjusted by velocity-based Courant–Friedrichs–Lewy (CFL), and a speed of sound based CFL set to below 0.15 and 2.0 respectively.

2.2.3 Boundary Conditions and Initial Set-up

The geometry of the experimental nozzle is determined using X-ray Computer-Aided Tomography (CAT) analysis as shown in Figure 2. This analysis reconstructs the images with the pixel number of 1016 × 1024 × 1024, and an effective voxel size of 2.318 µm.

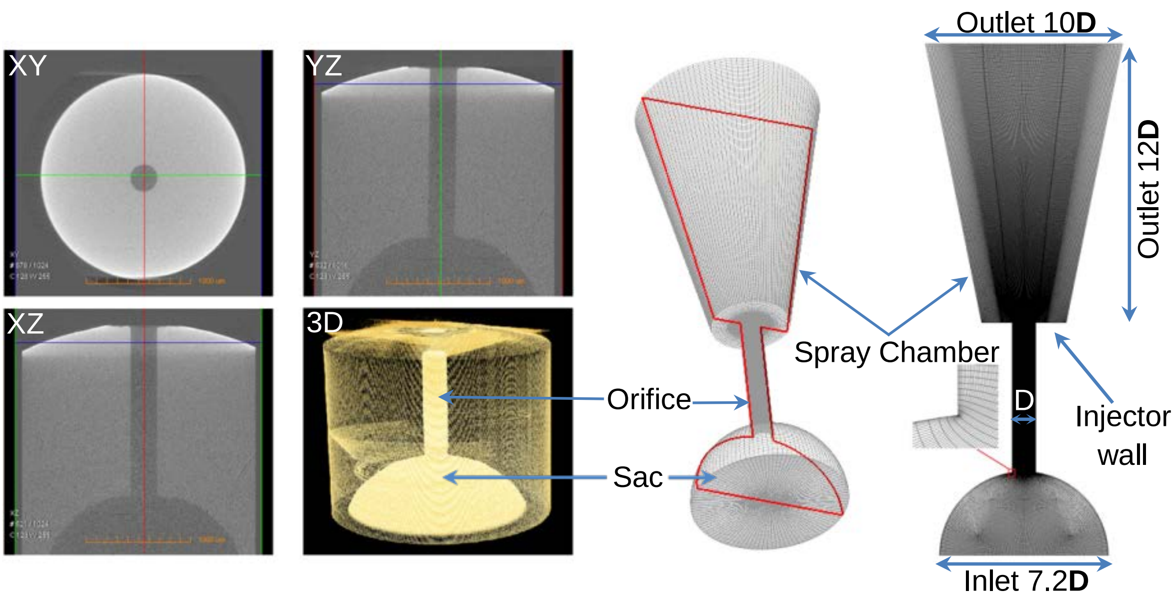

Figure 2. Left: X-Ray Tomography measurements of sac and orifice geometry conducted using an Xradia MicroXCT instrument by the Centre for Materials and Surface Science and the Centre of Excellence for Coherent X-ray Science at La Trobe University. Middle: the structured hexahedral mesh based on CAT measurements. Right: cross-section of the computational domain presents the mesh resolution, dimension and condition of the boundaries for coarse case with 4 million cells. The nozzle inlet is sharp edged.

All the experimental conditions are replicated in numerical models including the sac volume inlet, spray chamber pressure and air and diesel fuel temperature and viscosity. Fuel properties and set up conditions are listed in Table 1. In the absence of direct measurement, sac pressure is assumed to increase from chamber pressure (30 bar) to 850 bar after 50 μs then to 1200 bar after a further 25 μs then constant at 1200 bar to the end of simulation at 100 μs. This is to some extent arbitrary but is premised on published data implying that the sac pressure rises rapidly during needle opening [46, 58-60]. For instance, Moon et al. [46] found that the quasi-steady stage jet velocity was reached when the needle lift was only 17% of the maximum needle lift. The ramp is chosen to give an approximate match of modelled and experimental penetration rates. The lower pressure rise rate in the second 25 μs is adopted to avoid numerical instabilities.

Table 1. Fuel properties and operating conditions based on experimental setup.

Parameter	Value
Injection pressure	120 MPa average
Chamber pressure	30 bar
Nozzle diameter	0.25 mm
Nozzle length	1.6 mm
Nozzle nominal geometry	$K_S = 0$
Nozzle inlet radius	Sharp edged
Sac volume	0.19371 mm^3
Walls temperature	25°C
Fuel	Diesel
Fuel temperature	25°C
Fuel density	832 kg/m^3
Fuel Kinematic viscosity	$2.52 \times 10^{-6}\ m^2/s$
Fuel Re	$7\times10^3 \le Re_l \le 46\times10^3$
Fuel We	$4\times10^4 \le We_l \le 2\times10^6$
Gas	Compressed air
Gas temperature	25°C
Density ratio	42
Surface tension	0.03 N/m
*Indicative Injection velocity	367
*Fuel Mach number	367 / 1250 = 0.3
*Ohnesorge number	0.077

* Injection velocity, Mach and Ohnesorge numbers are for the developed spray, calculated based on experimental measurements [32]. The nozzle diameter is used as the length scale.

Fluid flow through the passage between the needle and seat is not modelled. In a real injector turbulence would develop in the needle/seat passage prior to the sac. This additional turbulence could contribute to more significant and earlier jet breakup. A pre-simulation approach could involve modelling the flow through the needle/seat passage in some fixed configuration, perhaps with the needle partially open and thus quantifying the turbulent flow field, which would then be used as an the initial condition at sac inlet. While this approach has merit, it is beyond the scope of the current work. A uniform pressure boundary with a turbulent intensity of 4.4% is applied over the sac entry plane. Thus, any effects due to turbulence or flow asymmetry generated in the passage between the needle and seat [60-64] are not modelled. A non-reflective boundary with the constant pressure of 30 bar is employed at the spray chamber domain. The nozzle and sac walls are adiabatic.

At the start of each injection in the experimentation, the nozzle is neither necessarily full nor empty of fuel due to the transient physics associated with the End of Injection (EOI) process from the previous injection event [47, 58-60]. The initial model conditions have the sac and 5.2D of the 6.4D long orifice (81% of the nozzle length) filled by diesel fuel at a pressure of 30 bar and the remainder of the nozzle filled with air. This initial stage is somewhat arbitrary and the rationale is described in Ghiji et al. [65].

A 3D hexahedral structured mesh with the non-slip boundary condition on the walls of the sac and nozzle is implemented to capture the non-axisymmetric nature of the injector flow and disintegrating jet [32, 42-44, 66], as shown in Figure 2. By generating a high grid resolution at the boundary layer of the nozzle walls, the utilization of a wall function has been obviated. Structured grids are used to achieve higher quality and control which may be sacrificed in unstructured and hybrid meshes. In addition, the efficiency of the differencing scheme for bounding the convection term of the transport equations in a structured mesh is much higher in comparison with an unstructured mesh [67].

A mesh sensitivity study is carried out using four mesh resolutions, very coarse (0.6 million cells), coarse (4 million cells), medium (8 million cells), and fine grid (20 million cells). The cell size is refined down to average 0.5 μm in the nozzle and 3 μm in the primary atomization zone for the fine mesh case. This cell size can capture droplets down to the 3 μm range based the optimistic premise that 5 cells can give a reasonable representation of a single droplet [14]. The resolution of these cases, time-step range, the number of CPUs, and computational cost (wall clock time) for each case are summarized in Table 2.

Table 2. Summary of meshes and computation parameters for numerical models. Total simulation time is 100 μs.

Case	**Average Spatial Resolution** (μm and cells/D)			**Cell count**	**Time Step** ($\times 10^{-9}$ S)	**CPU** (core count)	**Wall clock time** (hours)
	Sac	Orifice	Chamber				
Very Coarse	25 (20/**D**)	4 (65/**D**)	14 (20/**D**)	0.6×10^6	$1.5 \leq \Delta T \leq 30$	32	208
Coarse	13 (40/**D**)	2 (130/**D**)	6.5 (40/**D**)	4×10^6	$0.7 \leq \Delta T \leq 10$	128	501
Medium	7.5 (55/**D**)	1.2 (210/**D**)	5 (50/**D**)	8×10^6	$0.5 \leq \Delta T \leq 8$	256	739
Fine	4 (85/**D**)	0.5 (500/**D**)	3 (75/**D**)	20×10^6	$0.4 \leq \Delta T \leq 4$	512	965

3 Results and Discussions

3.1 Mesh Dependency and LES Quality

In order to take into account the significance of in-nozzle generated turbulence on primary atomization [13, 14], the size of the cells in the nozzle for the fine resolution case was decreased to the order of the Kolmogorov length scale $\eta = (\upsilon^3/\varepsilon)^{1/4}$ where ε is the average rate of dissipation of turbulence kinetic energy per unit mass. To resolve a given length scale η, the grid scale must be less than half of the length scale [57]. The smallest length scales associated with the flow field for the fully developed spray are reported in Table 3. It can be seen in this table that η_l in the nozzle is much larger than the mesh size for the finest mesh. This mesh resolution enables good prediction of small eddies of the liquid phase inside the nozzle. It was not possible to achieve mesh scales below the Kolmogorov length scale for the gas phase demonstrating the necessity for employing a sub-grid scale model to include turbulence effects in the gas phase.

Table 3. Kolmogorov length scales for the liquid and gas phases of the developed spray where the turbulence intensities used are 4.4% and 10%, respectively. The indicative injection velocity 367 m/s is used for these calculations.

Parameter	**Value** (μm)
Liquid phase Kolmogorov length scale, η_l	0.7
Minimum mesh size in the nozzle hole for fine case, Δx_{min}	0.1
Gas phase Kolmogorov length scale, η_g	0.1
Minimum mesh size in the spray chamber for fine case, Δx_{min}	1.7

The ratio of resolved turbulent kinetic energy (k_{res}) to total turbulent kinetic energy (TKE = k_{sgs}+ k_{res}) indicates the quality of the LES model and consequently the adequacy of the overall grid fineness [9, 68]. For satisfactory LES modelling this ratio should be more than 80% [68]. The resolved turbulent kinetic energy is calculated over 10 μs at a probe point located at 4D (1 mm) from the nozzle exit. The overall ratio of k_{sgs} to TKE predicted by the sub-grid scale turbulent model at the quasi-steady stage with the fine mesh resolution is equal to 2.4%. In addition, the numerical turbulent diffusion due to the discretization error is the same magnitude as the turbulent diffusion computed by the sub-grid scale model [9, 68]. Thus, at the quasi-steady stage with the finest grid, the resolved turbulent kinetic energy is calculated at 95.2 % of TKE indicating a satisfactory LES model.

Total pressure and mean velocity at nozzle exit were calculated for all meshes at the quasi-steady stage ($P_{injection}$ = 1200 bar) and the result is shown in Figure 3. The difference between the medium and the coarse mesh was in the order of 6.6%, while for the fine and the medium it was 1.1%.

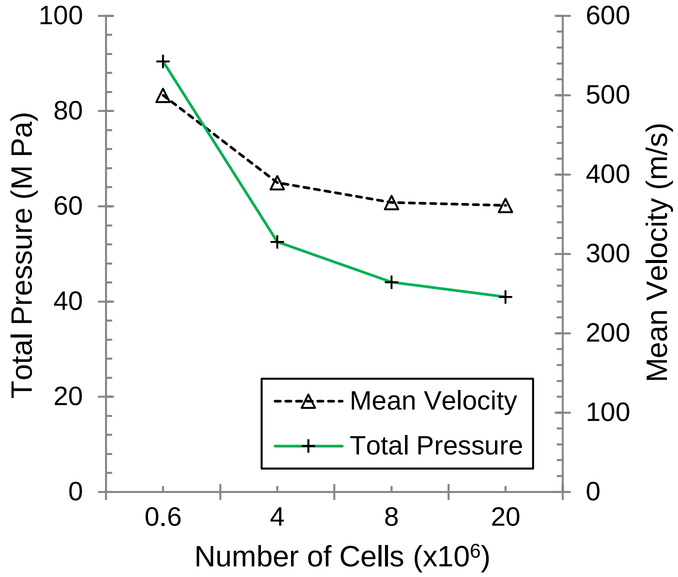

Figure 3. Comparison of total pressure and mean velocity for different mesh resolutions calculated on a cross-sectional plane at the nozzle hole exit, and the sac inlet pressure of 1200 bar.

Average radial profiles of absolute velocity magnitude and mass fraction of liquid at various distances from the nozzle hole inlet (1D, 2D, 4D, and 6.4D the end of the nozzle hole) for three meshes at the quasi-steady stage ($P_{injection}$ = 1200 bar) are shown in Figure 4. Maximum velocity of 480 m/s is captured at the centre of the nozzle (r/D=0) as expected. The average velocity and mass fraction at different locations inside the nozzle hole show tendency toward grid convergence for the finest mesh. The velocity on the nozzle wall (r/D=0.5) is zero as a result of the no-slip condition applied to the injector walls. The velocity of the layer of gas near the walls remains near zero until near the nozzle exit where inflow of gas from the chamber results in increased velocity magnitude. The gas layer thickness grows with distance from the nozzle inlet reaching at the nozzle exit around 70% of the cross-sectional area occupied by the liquid phase.

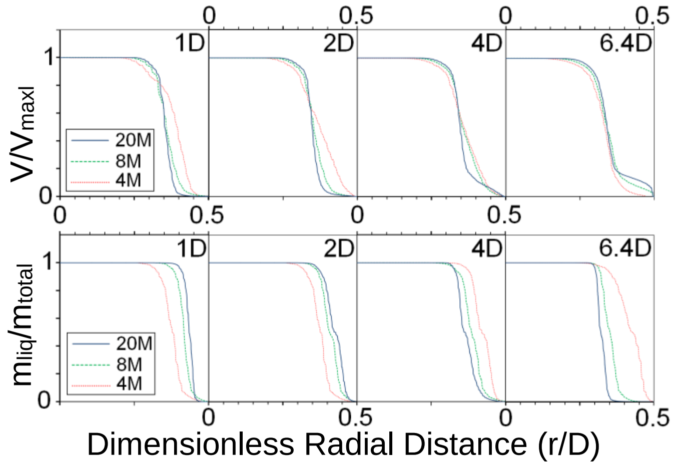

Figure 4. Averaged radial profiles of absolute velocity magnitude and liquid mass fraction on cross-sectional planes at 1D, 2D, 4D, 6.4D (end of the nozzle hole) from the nozzle hole inlet, at the quasi-steady stage. Maximum velocity is 480 m/s. The results show tendency to grid convergence for the finest mesh.

Probability density functions of droplet size for the entire domain outside the nozzle for each mesh density are shown in Figure 5. Both the droplet size range and the dominant size reduce with increasing mesh resolution. It can be seen however that both of these quantities show tendency to converge for the finest mesh. The probability density function for the fine mesh case demonstrates that the dominant droplet diameter captured is around 2.5 μm.

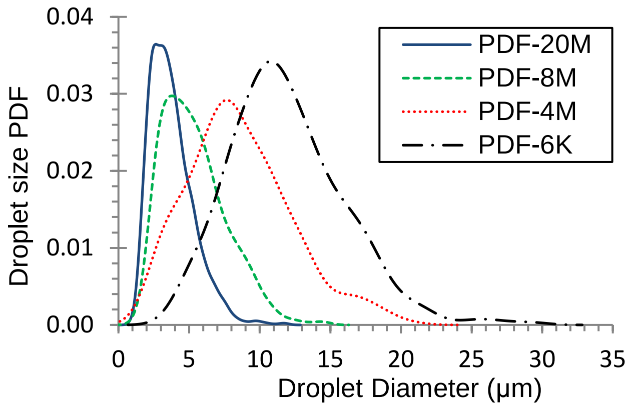

Figure 5. Probability density functions of droplet size for four mesh resolutions at the quasi-steady stage, demonstrating near convergence of dominant size and size range for the finest mesh.

The impact of mesh density on atomisation is shown with an instantaneous mass distribution of all droplets at various axial distances from the nozzle exit for three mesh resolutions at the quasi-steady stage of injection, presented in Figure 6. The value of total atomized mass is very small close to the nozzle exit, increases slowly up to 10D and then increases rapidly further downstream. Increasing the mesh density reduces the size of captured droplets, as shown in Figure 5, which consequently reduces the total mass of disintegrated liquid. Grid dependence of atomized mass increases with distance from the nozzle exit, due primarily to increasing grid size. The rest of the simulations presented in this paper are performed with the finest mesh. A still finer mesh was not considered practical due to limitations of the available computational power.

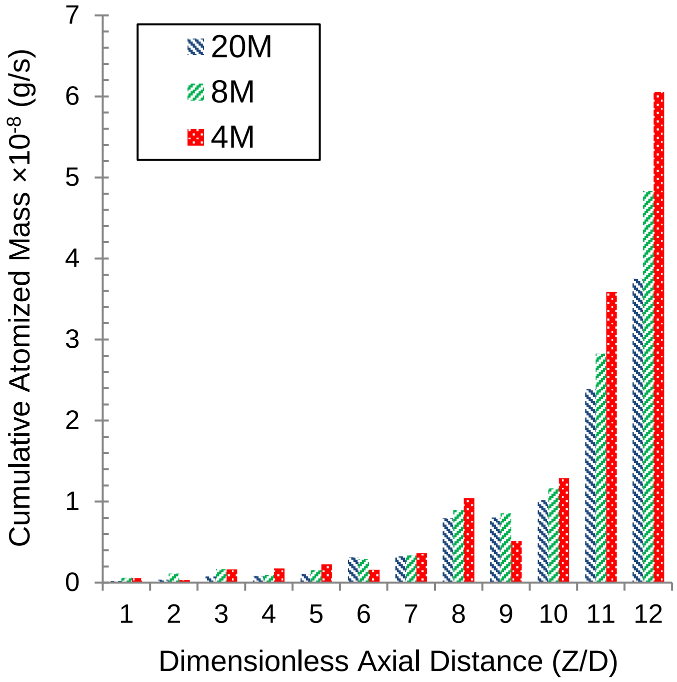

Figure 6. A snapshot of cumulative mass distribution of droplets along the axial distance from the nozzle exit for three mesh resolutions at the quasi-steady stage of injection. The value of total atomized mass is very small close to the nozzle exit, accelerates slowly up to 10D and then increases rapidly further downstream.

3.2 Mass Flow Rate

Mass flow rate and discharge coefficient at the nozzle exit predicted with the fine grid are shown in Figure 7. SOP is 12 μs after start of simulation and sac pressure reaches its maximum value of 120 MPa at 75 μs after start of simulation, so maximum sac pressure is reached at 63 μs ASOP. It can be seen in Figure 7 that modelled mass flow rate begins to level out at around 45 μs ASOP. The measured steady state flow rate and discharge coefficient for this injector are 0.0139 kg/s, and 0.6219 respectively [32] and the modelled values of 0.013 kg/s and 0.64 at the quasi-steady state are close to the measured values. The measured mass flow rate was found by repeatedly firing the injector for long opening times of 17 ms for more than 100 injection events, dividing the fuel consumed by the total time for which the injector needle was open. By this method, the time at which the injector needle is partially open is only a very small fraction of the total measurement time. There is an estimated ±10% uncertainty in measured mass flow rate so the modelled values agree within experimental error, giving confidence in the accuracy of applied numerical methods.

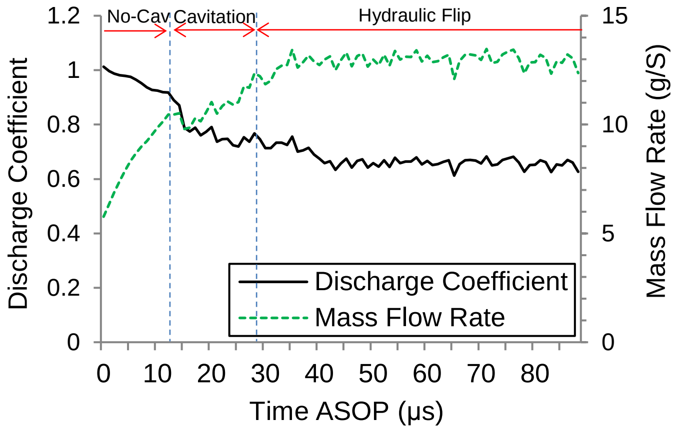

Figure 7. Discharge Coefficient (Cd) and total mass flow rate at the nozzle exit against time ASOP. The onset of cavitation occurs at 11 μs ASOP. The mass flow rate begins to level out at around 45 μs ASOP and reaches an average value of 0.013 kg/s in the quasi-steady stage.

The numerically predicted contraction coefficient is slightly higher than the theoretical limit for an ideal sharp entrance orifice ($C_c = \pi/(\pi+2) = 0.611$), with a value of $C_c = 0.619$.

3.3 Penetration Velocity

The Reynolds number and mean velocity of the flow at the nozzle exit for different times ASOP, predicted by the fine grid are presented in Figure 8. The mean velocity and Reynolds number increase up to around 100 MPa pressure difference then steady out at mean values of 480 m/s, and 46000 respectively. The displacement of the leading edge and time interval between shots are used to calculate penetration velocity, similar to the previous experimental studies [69-71], depicted in Figure 9. The jet leading edge is detected and distinguished from the image background using an intensity threshold criterion. A number of shots over a range of inter-frame times varying between 1 and 15 μs are analysed. The error bars are based on the accuracy of the detection of the leading edge of the jet and this is a function of the inter-frame time. The scatter in the experimental results demonstrates shot to shot variability in spray development. The jet penetration velocity at various axial distances from nozzle exit with corresponding time ASOP, demonstrated in Figure 9, show good agreement between numerical and experimental results.

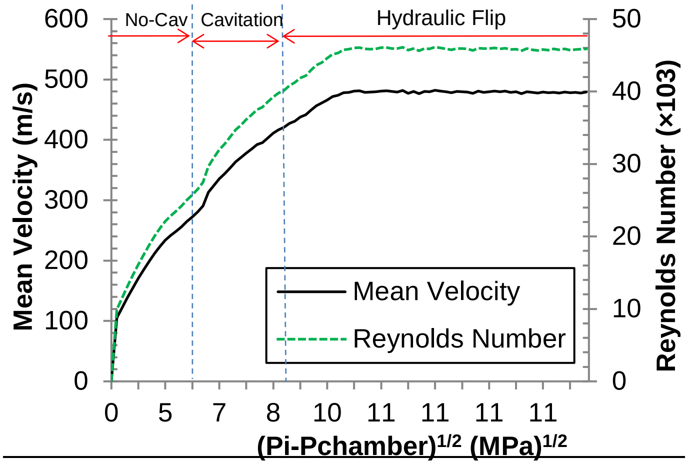

Figure 8. Mean velocity and Reynolds number of the the mixed-phase jet at the nozzle exit, against the square root of the difference between the sac pressure and the chamber pressure.

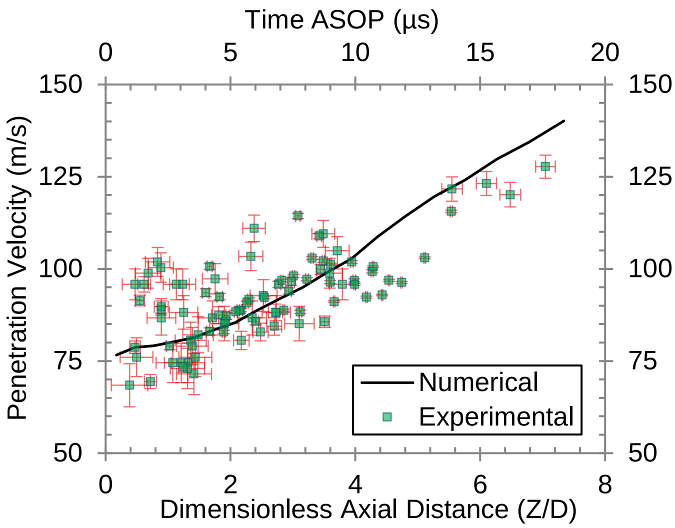

Figure 9. Experimental and numerical values of penetration velocity of the leading edge at various axial distances from the nozzle exit and time ASOP. The location of the leading edge at different times ASOP is correlated.

Uncertainties arise in these measurements from two dominant sources: variability in the measurement of spray image timing relative to SOP; and shot-to-shot variations in the spray dynamics. Due to uncertainties in acquiring an exact time of the start of injection, the penetration velocity of the jet was plotted against the location of the jet leading edge instead of the time after start of injection.

3.4 Evolution of Spray Structure

3.4.1 Morphology of Penetrating Jet during the early opening transient

Figure 10 shows a comparison of experimental images with the numerical results for the fine mesh case at different times ASOP using the 2× Barlow lens to give a total magnification of 7.7:1. Some transparency can be seen in the shadowgraphy images at the leading edge. This is thought to be due to air inclusion inside the nozzle, from the previous injection. The existence of ingested air inside the injector was reported by Swantek et al. [47]. The air inclusion inside the injector influences the spray structure and could be a source of the observed deviation between experimental and numerical results.

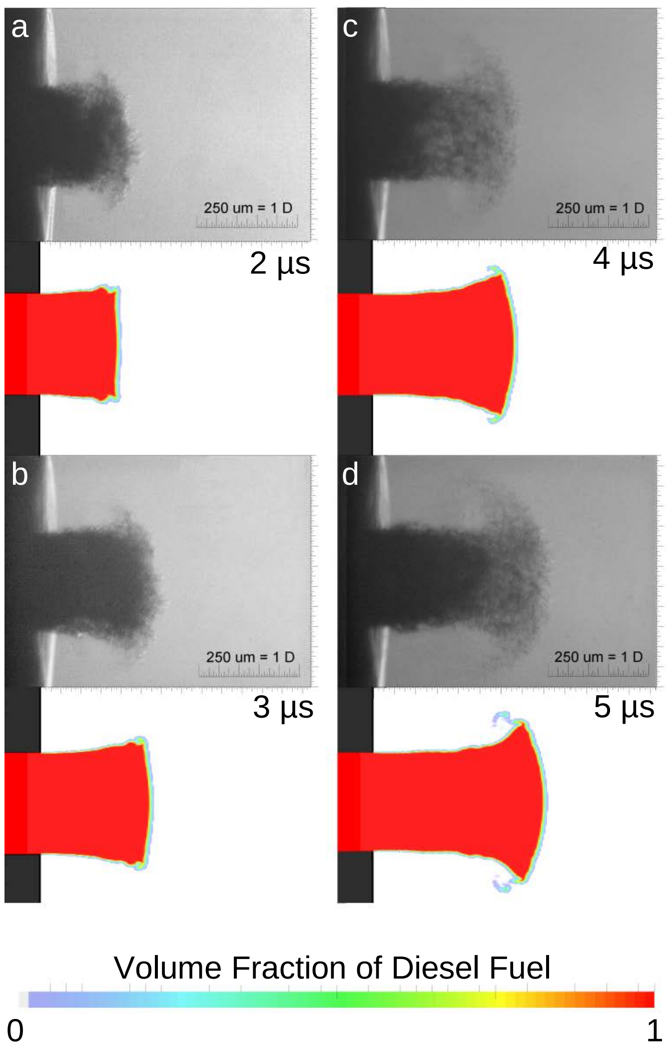

Figure 10. Comparison of experimental images with numerical results for the fine mesh case with the highest magnification. Each column of the experimental image is from a different injection event captured from two consecutive frames with 1 µs inter-frame time.

Consecutive images in (a) and (b) are from a single shot of the injector, while successive images in (c) and (d) are from another shot of the injector, each pair with 1 μs time interval. It is apparent in (c) and (d) that a liquid core is advancing into the dispersed leading edge. Numerical results show the structure of the jet colored by the volume fraction of diesel fuel (γ) at different times ASOP. Cells containing air only are shown in white.

The numerical and experimental results show the early development of the umbrella-shaped leading edge and the early stages of shedding of droplets from the rim of the leading edge. Shadowgraphy images with a larger field of view are compared with numerical results in Figure 11, presenting the general structure of the diesel spray. In this Figure, images (a) and (b), (d) and (e), (g) and (h), (i) and (j) are paired, each pair captured from a single injection event with 1 μs delay between two consecutive frames.

The necking of the jet behind the umbrella can be seen in the experimental images in Figure 11, while it is not marked in the simulations. The difference is possibly due to the presence of air in the experimental jet, as indicated by the partial transparency of the experimental images, and thus more rapid disintegration. The outer recirculating gas flow removes the generated droplets and advects them toward the outer flow. Another difference between the numerical and experimental results is in the production of very small droplets in the experimental images unlike them that in the simulations. This is due to the constraint in computational resources where the grid resolution in the computational domain is insufficient to resolve the small eddies in the gas phase which influences the breakup process of the ligaments and droplets.

The overall morphology of the early spray as modelled here taking into account compressibility is not significantly different from simulations assuming incompressible fluid as reported in Ghiji et al. [65]. This is because the Mach number of the liquid at this stage of the injection is less than 0.3 and thus compressibility effects are negligible. Further, cavitation is only just beginning. Cavitation is apparent with the formation of cavities on the walls just downstream of the nozzle entrance and the associated formation of cavitation bubbles.

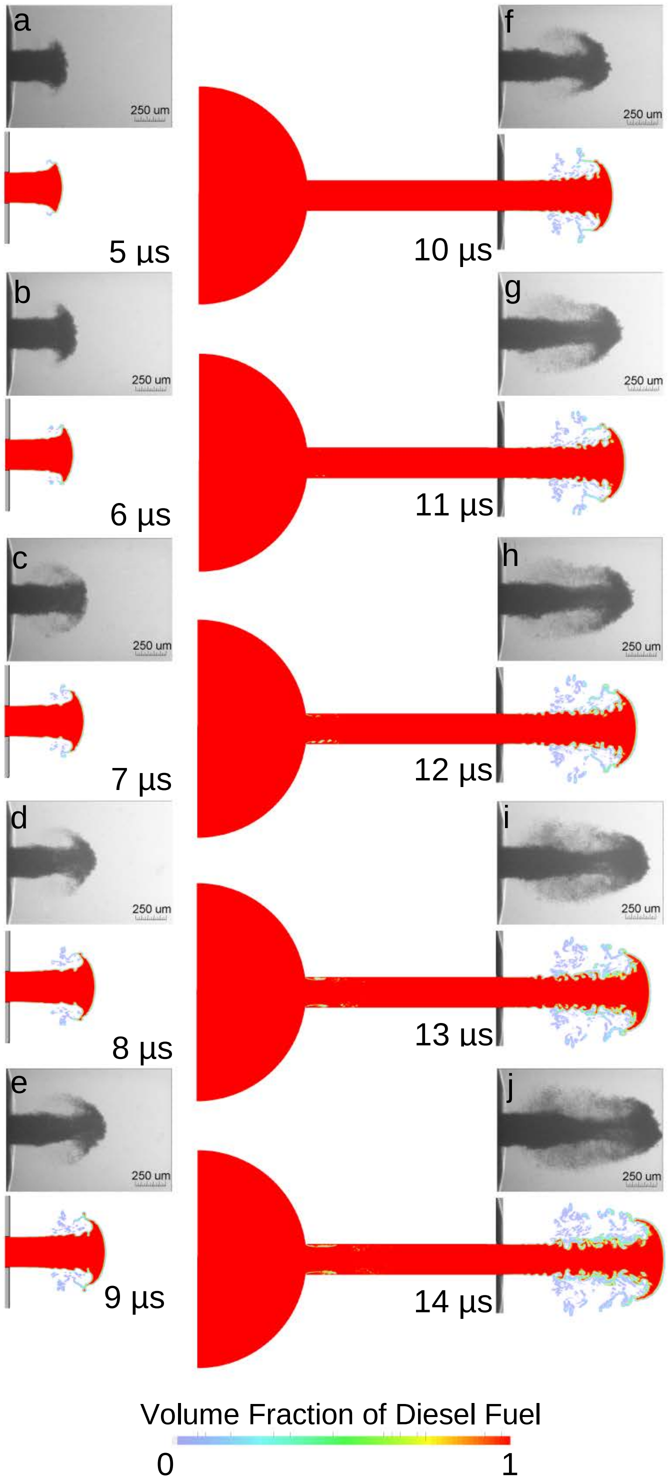

Figure 11. Comparison of experimental images with numerical results extracted from the fine case for the SOP process. Images a and b, d and e, g and h, i and j are paired, each pair captured from the same injection event with 1 µs inter-frame time. Numerical results show the structure of the liquid jet colored by γ at corresponding times ASOP. The onset of cavitation downstream of the nozzle entrance is apparent. Cavitation bubbles can be seen arising near the nozzle entrance which are then transported down the nozzle.

The onset of cavitation occurs at 11 μs ASOP where the pressure of diesel fuel drops to the diesel fuel vapour pressure, 1 kPa, just after the sharp edged nozzle hole inlet, as depicted in Figure 12. The development of cavities further downstream can be seen in images b, and c with their corresponding static pressure distribution illustrated in images f, and g respectively. At image d 27 μs ASOP, cavities extend to the end of nozzle hole while high-pressure spray chamber air penetrates into the gap between the nozzle wall and liquid jet interfaces.

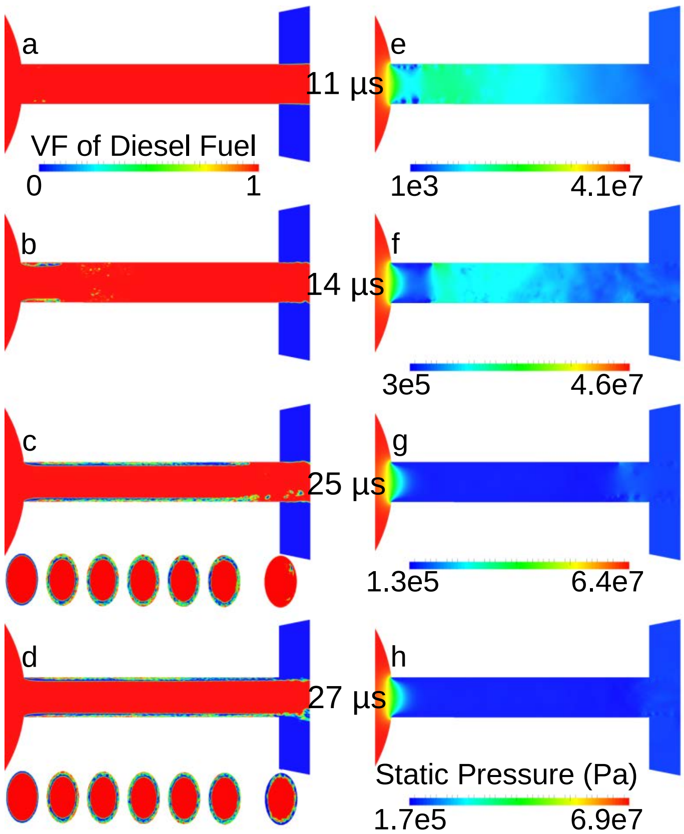

Figure 12. A zoomed-in view of the nozzle hole shows the onset and enhancement of cavitation at various times ASOP colored by the volume fraction of diesel fuel (images a-d), and static pressure (images e-h). The onset of cavitation can be seen in the image a where the static pressure of liquid drops to the liquid vapor pressure, 1000 Pa, in image e. Hydraulic flip, a detachment of liquid from the entire nozzle wall is depicted in images d, and h.

3.4.2 Evolution of in-nozzle and jet liquid-gas turbulent structures

3.4.2.1 Starting vortex

The experimental images show a toroidal vortex just behind the leading edge of the emerging spray within the first few microseconds of penetration. This structure is apparent due the density gradients in the chamber air inherent in the toroidal flow. Further, numerous experimental images show the vortex very close to the nozzle exit, prior to the emergence of liquid. This is thought to be due to the presence of air in the nozzle, with the air being ejected before the fuel and thus creating the shear-induced vortex, as seen in Figure 13 which illustrates the initial vortex formation in the gas phase experimentally (13-a) and numerically (13-b and c). The numerical result is shown at 2 μs Before Start Of Penetration (BSOP). A positive *Q*-criterion showing the small-scale turbulent structures where mixing is important is shown in Figure 13-c. The color in the *Q*-isosurface indicates the vorticity in the *z*-direction, red indicates clockwise rotation and blue counter clockwise rotation. The shots showing the vortex before the fuel appears are generally for earlier timing meaning that there is always air ejected first but this is only seen for the earliest timing of the images. The initial air slug seen experimentally is taken as further evidence of the existence of air in the nozzle prior to injection. In section 2.2.3 the inclusion of air as the initial condition is discussed. Modelled air density is also plotted in Figure 13 showing the density gradient associated with the starting vortex induced by the initial slug of air prior to liquid. It is likely that the amount of air in the nozzle and the configuration of the air-fuel interface vary from shot to shot.

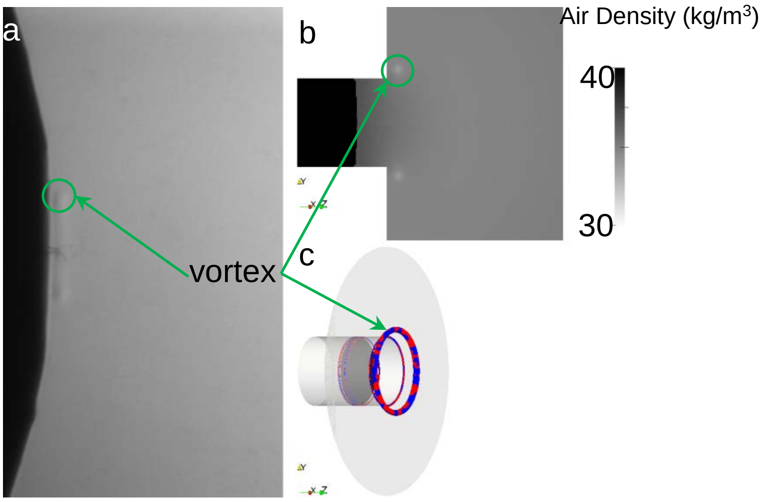

Figure 13. Starting vortex at or just before the start of penetration (BSOP); image a shows shadowgraphy result; image b and c depict the CFD results at 2 μs BSOP. Image b is shaded by air density on a centralized cut plane. Image c shows the Q-isosurface of 5×10^{12}, colored by vorticity in the z-direction, where red indicates clockwise rotation and blue counter clockwise rotation. The body of the injector is shown in light grey and the dark grey disc shows the location of the leading edge of the liquid (filtered by a liquid fraction of 0.5) relative to the vortical structures.

Figure 14 illustrates the initial vortex formation in the gas phase experimentally (14-a) and numerically (14-b and c) after the liquid has begun to penetrate. The numerical result is shown at 2 μs ASOP. A positive *Q*-criterion showing the small-scale turbulent structures where mixing is important is shown in Figure 14-c. The isosurface volume fraction of liquid $\gamma = 0.5$ is also shown in black to represent the location of the leading edge of the liquid relative to the vortical structures.

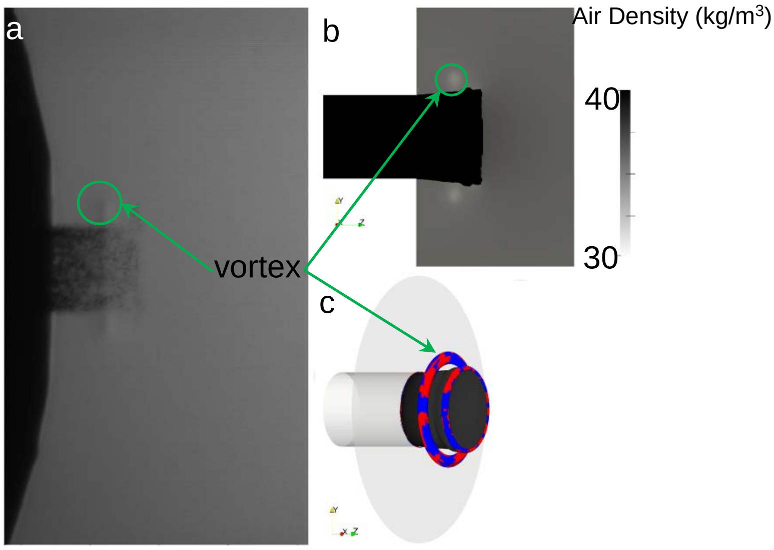

Figure 14. Starting vortex at the start of penetration; image a shows shadowgraphy result; images b and c depict the CFD results at 2 μs ASOP. Image b shows the starting vortex through the centralized cut plane, colored by air density range. Image c shows the Q-isosurface of 5×10^{12}, colored by vorticity in the z-direction, red indicates clockwise rotation and blue counter clockwise rotation. The body of the injector is shown in grey and the black color shows the location of the leading edge of the liquid (filtered by a liquid fraction of 0.5) relative to the vortical structures.

The jet and vortex propagation velocities are compared in Figure 15. Experimental values are shown for 16 different double frame shots, with 1, 2 or 3 μs inter-frame time. The error bars are based on the accuracy of the detection of the leading edge of the jet and the centre of the vortex. Predicted liquid and vortex propagation rates are also plotted. The modelled vortex propagation rate is found by integrating velocity over the Q-criterion isosurface of 5×10^{12}. The dip in the modelled vortex penetration rate around $Z/D = 0.4$ corresponds to the time when the fuel leading edge reaches the vortex. It can be seen that the vortex propagation rate is approximately 40% of the jet leading edge propagation rate on average. The liquid propagation rate shows good agreement between experiment and model, while greater differences are seen between the experimental and modelled vortex propagation rate. The source of the variation in the measured results and the differences between the measured and modelled results are most likely due to variability in the location of the air-fuel interface inside the orifice prior to injection.

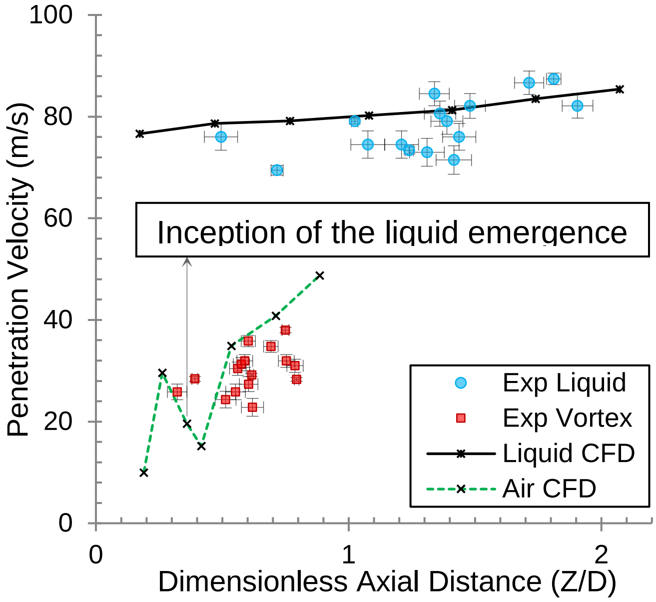

Figure 15. Experimental measurements of penetration velocity for the jet leading edge and the starting vortex at a different distance from nozzle hole exit.

3.4.2.2 Effects of cavitation and in-nozzle turbulence on spray development

The computed spray structure at various times ASOP is illustrated in Figure 16. In the left column (a-f), the fluid in the sac and nozzle is colored by velocity magnitude and the 0.5 liquid volume fraction isosurface in the chamber is colored by turbulent kinetic energy. In the right column (g-l), turbulent structures are depicted using the *Q*-criterion isosurface of 5×10^{12} colored by vorticity magnitude (for a clearer presentation, high value 2×10^{8} of vorticity at the sharp edged nozzle hole inlet has been excluded).

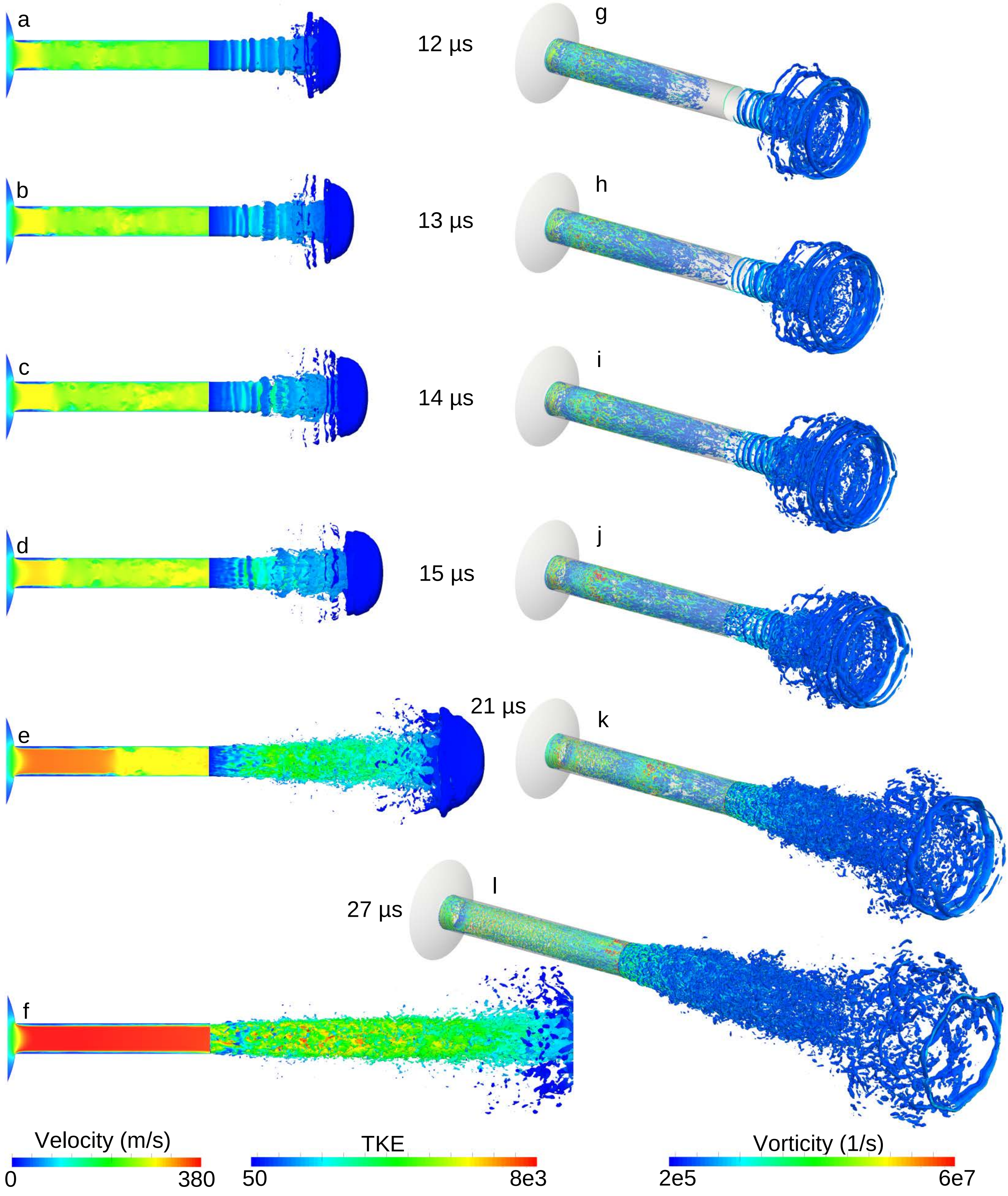

Figure 16. Evolution of in-nozzle and jet liquid-gas turbulent structures at different times ASOP. In the left column (image a-f), in-nozzle flow is colored by velocity magnitude; liquid-gas isosurface of 0.5 at the spray chamber is

colored by Turbulent Kinetic Energy (TKE). In the right column at corresponding times (image g-l), the development of turbulence is illustrated using Q-isosurface of 5×10^{12}, colored by vorticity magnitude (for a clearer presentation, the high value of vorticity of 2×10^{8} at the sharp edged nozzle hole inlet has been excluded).

At 12 µs ASOP, Figure 16-a, g, toroidal streamwise waves are apparent at the gas-liquid interface in the vicinity of the nozzle exit. These waves are also apparent as coherent toroidal structures in the Q-plot. The jet leading edge velocity is 105 m/s and the velocity at nozzle exit is 198 m/s corresponding to a Reynolds Number of 9930 and 18720, respectively. These streamwise waves could be potentially generated due to either Kelvin-Helmholtz instability or 2D Tollmien-Schlichting instability as recently reported by Shinjo et.al [72]. The turbulence generated primarily at the sharp nozzle inlet but also in the boundary layer develops with an increase in nozzle velocity. Cavitation onset occurred at 11 µs ASOP.

Experimentally, the streamwise waves were difficult to capture in the image due to the obscuration of the jet surface by the cloud of fine droplets generated in the early stages of injection. In Figure 17, a streamwise surface waveform is just apparent on the top edge near the edge of the obscuring outer cloud of fine droplets.

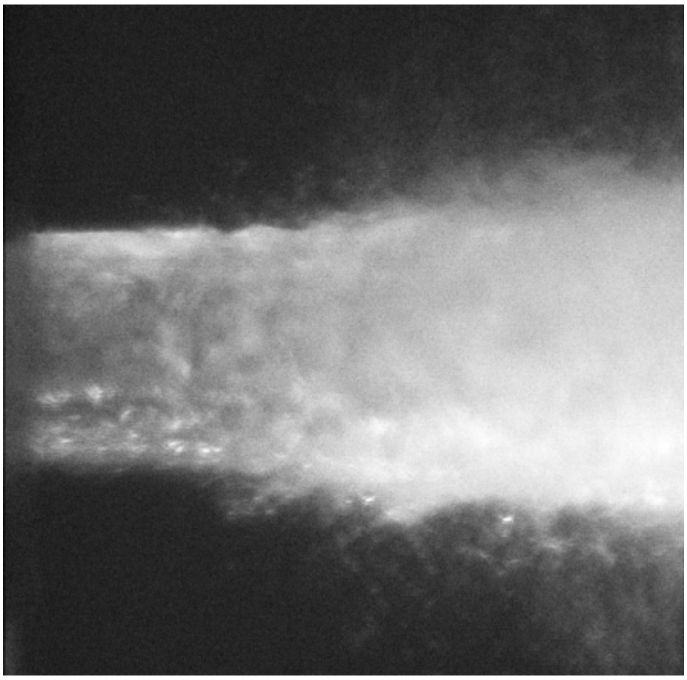

Figure 17. Experimental image of a spray near the nozzle using a diffuse sidelight imaging technique. A streamwise surface waveform is just apparent on the top edge near the edge of the obscuring outer cloud of fine droplets.

At 13 μs ASOP, Figure 16-b, h, the vapor cavities are developing and extending downstream inside the orifice, moderating the turbulence generated at the nozzle entrance and in the boundary layer. The influence of detachment can be seen in Figure 16-b This is due to the increase in velocity at the nozzle entrance (extension of yellow color further downstream of the nozzle) as a result of the reduction in cross-sectional area, similar results are reported by Dumont et al. [73], Desantes et al. [74], and Benajes et al. [75]. The developing in-nozzle turbulence is characterized by apparent streamwise, stretched vortices upstream of the nozzle exit. The toroidal streamwise waves on the jet are increasing in amplitude, possibly due to the increased upstream flow velocity. The disintegration of these waves tends to occur closer to the nozzle exit as the jet accelerates.

At 14 μs ASOP, Figure 16-c, i, the amplitude of the toroidal streamwise waves further increases. In-nozzle vortical structures have not yet reached the chamber. Onset, growth, and disintegration of the streamwise toroidal waves continues to occur closer to the nozzle exit as the jet accelerates. Figure 18 shows the liquid volume fraction isosurface of 0.5, colored by the velocity magnitude at 13.9 μs ASOP. Instabilities form on the emerging jet, and then develop into surface waves ultimately breaking up with downstream propagation. The zoomed views, 0.1 μs apart, show a typical ligament and its subsequent breakup into droplets, as part of the process of surface wave breakup. It can be seen that irregularities on the trailing edge of the umbrella play a significant role in the disintegration process. The separation of filaments from the trailing edge of the jet tip and their fragmentations lead to the generation of large droplets at the early stage of injection. An animation of the surface wave development between 12 ASOP and 15 ASOP is given in the supplementary material. It demonstrates the propagation of the toroidal streamwise waves in the downstream direction and the stretching of the leading edge umbrella prior to the shedding of droplets.

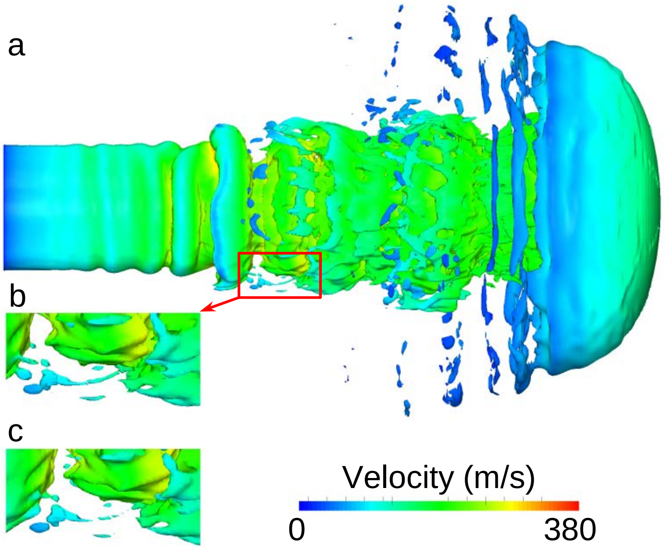

Figure 18. A view of surface instabilities forming surface waves that break up with their downstream propagation, filtered by the liquid volume fraction isosurface of 0.5, colored by velocity magnitude at 13.9 µs ASOP. The separation of filaments from the trailing edge of the jet tip and their fragmentation are apparent. The zoomed-in views show the breakup of a filament between 13.9 µs (b), and 14 µs (c) ASOP.

At 15 µs ASOP, Figure 16-d, j, the impact of cavitation lowering the turbulence level at the nozzle entrance can be clearly seen in the Q criterion plot, about 2 nozzle diameters downstream of the nozzle entrance. Further downstream, longitudinal vortical structures formed earlier emerge from the nozzle exit coinciding with the appearance of spanwise longitudinal waves on the jet surface near the nozzle exit. By 15 µs the coherent toroidal streamwise waves have disappeared, replaced by hairpin vortices at 16 µs.

At 21 µs ASOP, Figure 16-e, k, the vapor cavities have extended to the middle of the nozzle where a distinctive decrement in the jet velocity is apparent. Much greater disintegration of the jet occurs at this stage corresponding to the influence of the in-nozzle turbulence creating surface disturbances that promote instability and breakup. The Q criterion visualization, Figure 16-k, shows the growth in the thickness of the shear layer (mixing zones) about the jet periphery and umbrella shaped leading edge.

At 27 µs ASOP, Figure 16-f, l, the nozzle cavity reaches the nozzle exit and hydraulic flip ensues. In-nozzle turbulence production is significantly reduced with jet detachment from the nozzle sharp entrance no longer being affected by the nozzle wall. Turbulence production, however, remains due to flow contraction at nozzle entrance as apparent from the Q criterion visualization. The jet flow contraction associated with flow detachment at the nozzle entrance creates a momentary velocity decrease as shown in Figure 16-l. Beyond this stage, the jet approaches the quasi-steady stage with surface breakup rapidly commencing within a diameter from the nozzle exit.

The spatial distribution of droplet size and Weber number of each droplet outside the nozzle at the quasi-steady stage for the fine mesh resolution is shown in Figure 19. The 3D surface is constructed based on the location and diameter of all droplets colored by their Weber number. At the edge of the jet, the droplet sizes are small and Weber numbers are large due to the high velocity of droplets just separated from the liquid core. The droplet sizes increase with increasing streamwise and radial distances as the velocities and Weber numbers decrease. Each peak on the surface is an individual droplet (2700 in total) from which the volumetric concentration can be seen to decrease with increasing streamwise and radial distances.

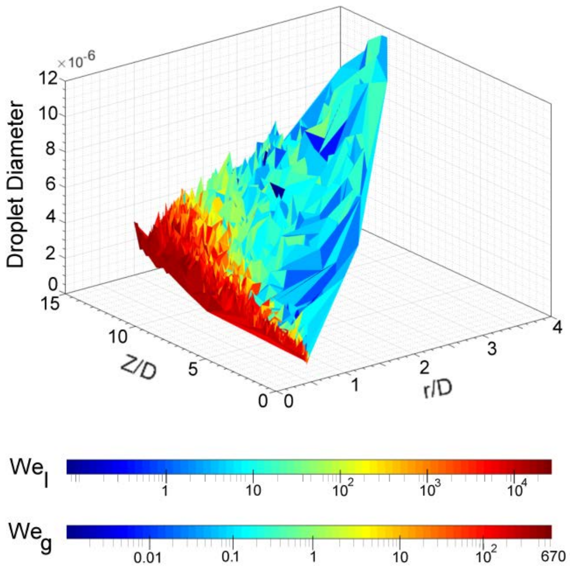

Figure 19. The spatial distribution of droplet size and Weber number of each droplet outside the nozzle at the quasi-steady stage for the fine mesh (20 million cells). The 3D surface is constructed based on the location and diameter of all 2700 droplets and colored by their Weber number. The Weber number of each droplet is calculated based on the density of droplet (We_l) and the density of gas (We_g). It can be seen that the droplet sizes increase with increasing streamwise and radial distances as the velocities and Weber numbers decrease.

3.5 Shock Waves

By 27 µs ASOP, shock waves begin to appear in both the experimental and modelled results. The onset of shock waves also corresponds to the modelled onset of hydraulic flip, where vapour cavities initiated at the nozzle entrance extend to the full nozzle length and become ventilated with the chamber gas. This may be a coincidence but both are the result of increased nozzle exit velocity as the needle lift increases and the sac pressure builds towards its maximum value.

Figure 20 shows the experimental and computed images at the onset of shock waves and beyond. The first column (images a and b) shows the montaged images of shock waves edges, extracted using an edge detection algorithm in MATLAB, superimposed on the experimental results. The second column (images c and d) illustrates the numerical results. The white areas represent cells which have a liquid fraction greater than 0.1. Image (a) at 27 μs ± 2 μs ASOP shows the first signs of the onset of shock waves, while image (b) at 37 μs ± 2 μs, shows further development of shock waves than the image (a). Each of these images is obtained from separate shots. Numerous shots confirm the onset of shock waves at about 27 μs ASOP. The timing technique used here is explained in section 2.1. The shock waves at the time of onset are seen to be most marked near the nozzle exit where the jet surface velocity is the highest. The numerical results presented in the image (c) show the onset of shock waves at essentially the same time ASOP and over a similar spatial extent to the measurements. An increase of about 15-25% of the air density at each shock wave front can be seen in images (c) and (d).

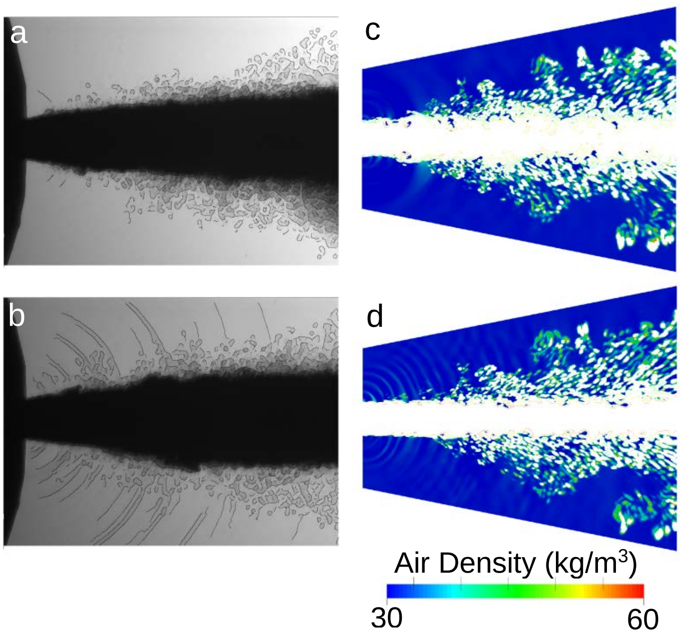

Figure 20. The onset of shock waves. The frames a and b (first column) are the montaged experimental images and an edge detection procedure applied to the experimental results. The frames c and d, second column, illustrate the numerical results at 27 μs, and 37 μs ASOP, respectively. The white areas represent cells which have a liquid fraction greater than 0.1. The density range is adjusted to highlight the shock waves.

The method used for measurement of the interfacial velocity is similar to that employed by Hillamo et al. [34]. It is assumed that the shock waves are initiated at disturbances on the interface between the liquid jet and the chamber gas where the interface velocity exceeds the local speed of sound. The Mach number, Ma of the jet interface may be derived from the angle of the shock wave relative to the interface, α, from the relation Ma = 1/Sin α. Ma is defined as the ratio of the interface velocity to the local speed of sound in the gas phase [76]. The local speed of sound in the chamber gas at the test conditions of 298 K and 30 bar is about 348 m/s. The Ma applicable to each shock wave in the experimental images is calculated and the results are shown in Figure 21 and 22 against axial distance from the nozzle. Errors involved in the shock waves angle measurement basically originate from the method applied for drawing each line of the angle. One line of this angle indicates the interfacial surface of liquid-air and another line is the shock wave tangent. The main error in this measurement corresponds to the averaging approach used to draw the edge representing the interfacial surface. The value of this error decreases further downstream as the deviation of the averaged line from exact interfacial edge diminishes due to the lesser interface instabilities. Figure 21 shows data for various times ASOP during the spray transient, while Figure 22 shows data for a single shot during the quasi-steady stage ($P_{injection}$ = 1200 bar).

For comparison with the experimentally derived interface velocity, the computed interface velocity is extracted from the outer isosurface of the jet with 0.5 liquid fractions. This interface velocity is also plotted in Figure 21 and 22. For the numerical results, the location of the shock waves imaged in Figure 20 correspond to peaks of computed interface velocity in excess of Ma = 1 shown in Figure 21. At 27 μs ASOP, the Ma of three experimentally imaged shock waves, shown in Figure 20a, are measured and plotted in Figure 21. At 32 μs ASOP, the number of shock waves captured increased which is evidence of an increase in the liquid jet velocity. The occurrence of shock waves is extended to 3.8 and 7.5 nozzle diameters downstream for experimental and numerical results respectively. At 37 μs ASOP, an increase in the number and extent of the shock waves is captured both in the experimental and numerical results.

The main source of deviation between experimental and numerical results could be related to not only the different calculation method but also the accuracy of the experimental shock wave capturing technique which employed backlit imaging. This technique suffers from obscuration by the cloud of fine droplets surrounding the spray.

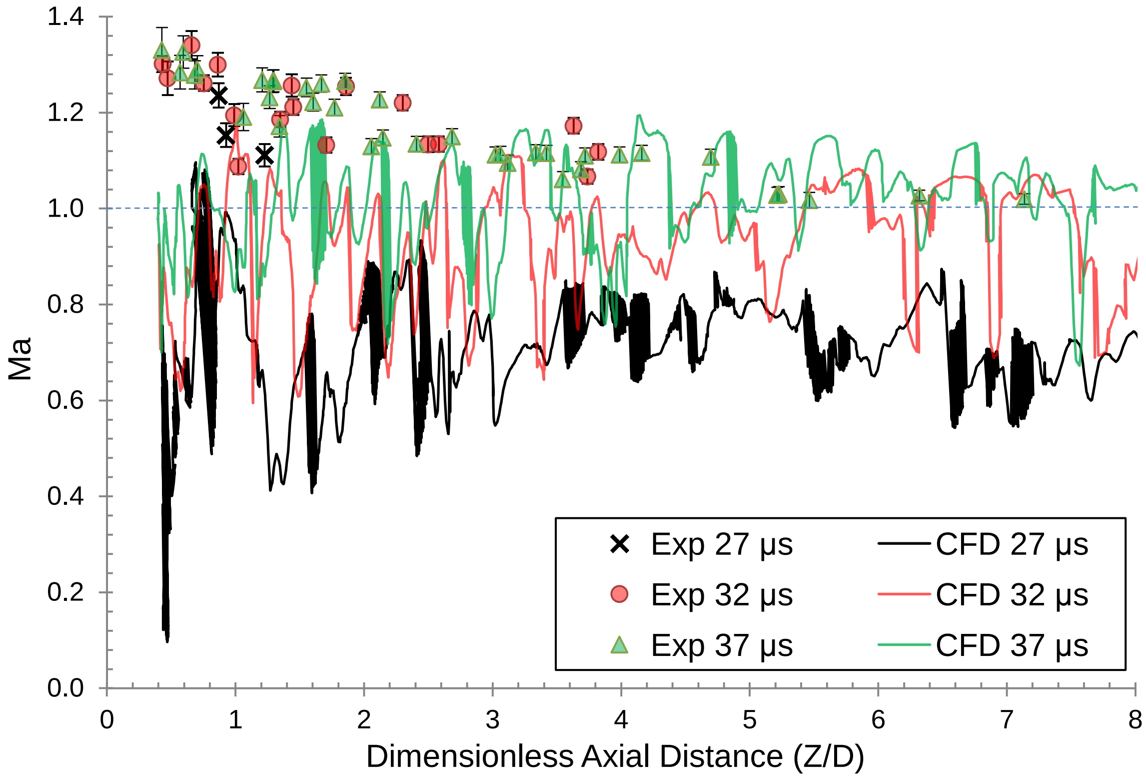

Figure 21. Experimental and numerical liquid-gas interface Mach number against axial distance from the nozzle exit, at various times ASOP. As the jet accelerates, the number of shock waves increases. The jet velocity has not yet reached steady stage.

As shown in Figure 8, sometime after the opening transient, at around 45 μs ASOP, the modelled nozzle exit velocity approaches the quasi-steady stage. At this stage, the shock waves are captured furthest downstream as demonstrated in Figure 22. The numerical jet interface velocity is high enough to generate the shock waves all the way downstream. Based on the jet diameter and liquid density, Weber number of the liquid-gas interface (We_{l}) is calculated, varying from 0.5×10^6 to 2×10^6. The fluctuation in the jet interface velocity both in experimental and numerical results thought to be due to surface instabilities on liquid-air interfaces.

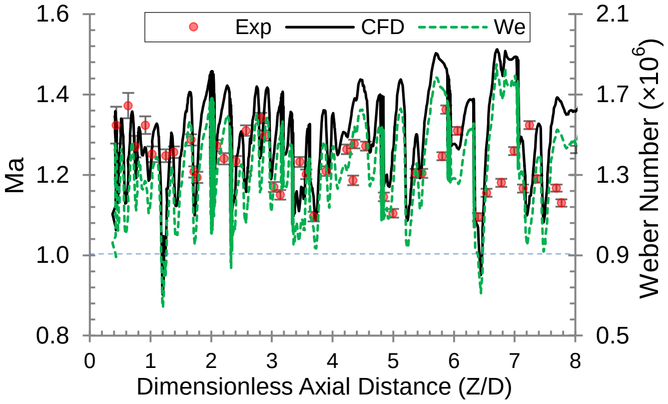

Figure 22. Experimental and numerical liquid-gas interface Mach and Weber number against axial distance from the nozzle exit after the jet has reached the quasi-steady stage ($P_{injection}$ = 1200 bar). Based on the jet diameter, Weber number is calculated which is in the range of $0.5\times10^6 \leq We_l \leq 2\times10^6$ ($12\times10^3 \leq We_g \leq 48\times10^3$).

4 Conclusions

The early stage of diesel spray dynamics is investigated experimentally and numerically employing microscopic backlit imaging and Eulerian/LES/VOF modelling respectively. Compressibility, temperature and cavitation effects for the liquid phase are included in the numerical model.

Mesh independency tests are conducted. Mean jet velocity, total pressure at nozzle exit and average radial profiles of velocity and mass fraction in the nozzle show tendency to convergence for the finest grid. At the quasi-steady stage, predicted mass flow rate matches experimental mass flow rate within experimental error. Comparison of measured penetration velocity of the jet between more than 100 consecutive shots and numerical results shows good correlation.

The effects of cavitation and in-nozzle turbulence on the growth and disintegration of surface structures on the emerging jet are characterized providing insight into the physics of primary atomization. At the start of penetration, an umbrella-like leading edge is captured in both the numerical and experimental data however only the experimental images demonstrate a semi-transparent cloud of air-fuel mixture at the leading edge. Initially, toroidal streamwise waves develop on the jet surface, travel downstream towards the leading edge umbrella and grow in magnitude until disintegrating in the wake. Subsequently, the emergence of longitudinal spanwise waves from the nozzle is accompanied by the disintegration of the toroidal streamwise waves, production of hairpin vortices and radial expansion of the jet mixing layer.

The first published experimental images of a starting vortex close to the nozzle exit at the start of injection, correlated with numerical results, are reported. The appearance of the starting vortex close to the nozzle exit before fuel penetration is taken as evidence of air inclusion in the nozzle. The location and velocity of the starting vortex are investigated experimentally and numerically. The vortex propagates downstream at about 40% of the jet penetration velocity

The onset and development of shock waves is presented experimentally and numerically and the jet interface velocity is inferred from the shock wave angle. This comparison shows good agreement between experimental and numerical results. The numerical results support the conclusion that shock waves occur where the jet velocity at the interface with the surrounding air exceeds the local speed of sound.

In order to cover the entire cycle of an injection, future studies could be directed to achieve a clearer insight into the physics involved during and after the end of injection process.

5 Acknowledgment

This work was supported by the Australian Maritime College and the Defence Science and Technology Group of Australia. We would like to acknowledge the use of the high performance computing facilities provided by the Tasmanian Partnership for Advanced Computing (TPAC) funded and hosted by the University of Tasmania. The authors express their gratitude to Luciano Mason, Mohammadmahdi Abaei, Hongjiang Yu, and Rouzbeh Abbassi for their support and suggestions.

6 Bibliography

[1] H. Hiroyasu, M. Arai, Structures of fuel sprays in diesel engines, in, SAE Technical Paper, 1990.

[2] S.N. Soid, Z.A. Zainal, Spray and combustion characterization for internal combustion engines using optical measuring techniques – A review, Energy, 36 (2011) 724-741.

[3] X. Jiang, G.A. Siamas, K. Jagus, T.G. Karayiannis, Physical modelling and advanced simulations of gas–liquid two-phase jet flows in atomization and sprays, Progress in Energy and Combustion Science, 36 (2010) 131-167.

[4] B. Mohan, W. Yang, W. Yu, Effect of internal nozzle flow and thermo-physical properties on spray characteristics of methyl esters, Applied Energy, 129 (2014) 123-134.

[5] S. Som, A.I. Ramirez, D.E. Longman, S.K. Aggarwal, Effect of nozzle orifice geometry on spray, combustion, and emission characteristics under diesel engine conditions, Fuel, 90 (2011) 1267-1276.

[6] X. Wang, Z. Huang, W. Zhang, O.A. Kuti, K. Nishida, Effects of ultra-high injection pressure and micro-hole nozzle on flame structure and soot formation of impinging diesel spray, Applied Energy, 88 (2011) 1620-1628.

[7] W. Huang, Z. Wu, Y. Gao, L. Zhang, Effect of shock waves on the evolution of high-pressure fuel jets, Applied Energy, 159 (2015) 442-448.

[8] T. Jin, K. Luo, Q. Dai, J. Fan, Direct numerical simulation on supersonic turbulent reacting and non-reacting spray jet in heated coflow, Fuel, 164 (2016) 267-276.

[9] O. Kaario, V. Vuorinen, T. Hulkkonen, K. Keskinen, M. Nuutinen, M. Larmi, F.X. Tanner, Large Eddy Simulation of High Gas Density Effects in Fuel Sprays, Atomization and Sprays, 23 (2013).

[10] R. Gjesing, J.H. Hattel, U. Fritsching, Coupled atomization and spray modelling in the spray forming process using openfoam, Engineering Applications of Computational Fluid Mechanics, 3 (2009) 471-486.

[11] C. Baumgarten, Mixture formation in internal combustion engines, Springer, Germany, 2006.

[12] M. Gorokhovski, M. Herrmann, Modeling primary atomization, Annu. Rev. Fluid Mech., 40 (2008) 343-366.

[13] L. Bravo, C. Ivey, D. Kim, S. Bose, High-fidelity simulation of atomization in diesel engine sprays, in: Proceedings of the Summer Program, 2014, pp. 89.

[14] M. Herrmann, On simulating primary atomization using the refined level set grid method, Atomization and Sprays, 21 (2011) 283-301.

[15] M. Stahl, M. Gnirß, N. Damaschke, C. Tropea, Laser Doppler measurements of nozzle flow and optical characterisation of the generated spray, in: ILASS, Orleans, France, 2005.

[16] G.M. Faeth, L.P. Hsiang, P.K. Wu, Structure and breakup properties of sprays, International Journal of Multiphase Flow, 21 (1995) 99-127.

[17] P.K. Wu, L.K. Tseng, G.M. Faeth, Primary breakup in gas/liquid mixing layers for turbulent liquids, Atomization and Sprays, 2 (1992).

[18] R. Domann, Y. Hardalupas, Breakup model for accelerating liquid jets, in: Proceedings of 42nd AIAA Aerospace Science Meeting and Exhibition, 2004.

[19] C. Badock, R. Wirth, A. Fath, A. Leipertz, Investigation of cavitation in real size diesel injection nozzles, International Journal of Heat and Fluid Flow, 20 (1999) 538-544.

[20] C. Arcoumanis, H. Flora, M. Gavaises, M. Badami, Cavitation in real-size multi-hole diesel injector nozzles, SAE Trans., J. Engines, 109 (2000) 3.

[21] H. Chaves, C.H. Ludwig, Characterization of cavitation in transparent nozzles depending on the nozzle geometry, in: Proc. Annu. Conf. Inst. Liq. Atom. Spray Syst., 18th (ILASS-2005), Orleans, France, 2005, pp. 259-264.

[22] M. Stahl, N. Damaschke, C. Tropea, Experimental investigation of turbulence and cavitation inside a pressure atomizer and optical characterization of the generated spray, in: Proceedings of international conference on liquid atomization and spray systems, 10th ICLASS, Kyoto, Japan, Paper, 2006.

[23] C.M. Varga, J.C. Lasheras, E.J. Hopfinger, Initial breakup of a small-diameter liquid jet by a high-speed gas stream, Journal of Fluid Mechanics, 497 (2003) 405-434.

[24] A. Sou, S. Hosokawa, A. Tomiyama, Effects of cavitation in a nozzle on liquid jet atomization, International Journal of Heat and Mass Transfer, 50 (2007) 3575-3582.

[25] Y. Wang, L. Qiu, R.D. Reitz, R. Diwakar, Simulating cavitating liquid jets using a compressible and equilibrium two-phase flow solver, International Journal of Multiphase Flow, 63 (2014) 52-67.

[26] W. Nurick, Orifice cavitation and its effect on spray mixing, Journal of fluids engineering, 98 (1976) 681-687.

[27] A. Lefebvre, Atomization and sprays, CRC press, 1988.

[28] R. Payri, J.P. Viera, V. Gopalakrishnan, P.G. Szymkowicz, The effect of nozzle geometry over internal flow and spray formation for three different fuels, Fuel, 183 (2016) 20-33.

[29] R. Payri, F. Salvador, J. Gimeno, O. Venegas, Study of cavitation phenomenon using different fuels in a transparent nozzle by hydraulic characterization and visualization, Experimental Thermal and Fluid Science, 44 (2013) 235-244.

[30] J.M. Desantes, R. Payri, A. García, J. Manin, Experimental study of biodiesel blends' effects on diesel injection processes, Energy & Fuels, 23 (2009) 3227-3235.

[31] M. Battistoni, C. Grimaldi, F. Mariani, Coupled simulation of nozzle flow and spray formation using diesel and biodiesel for ci engine applications, in, SAE Technical Paper, 2012.

[32] L. Goldsworthy, C.H. Bong, P.A. Brandner, Measurements of diesel spray dynamics and the influence of fuel viscosity using PIV and shadowgraphy, Atomization and Sprays, 21 (2011).

[33] T. Nakahira, M. Komori, M. Nishida, K. Tsujimura, The shock wave generation around the diesel fuel spray with high pressure injection, in, SAE Technical Paper, 1992.

[34] H. Hillamo, T. Sarjovaara, O. Kaario, V. Vuorinen, M. Larmi, Diesel spray visualization and shockwaves, Atomization and Sprays, 20 (2010).

[35] A.G. MacPhee, M.W. Tate, C.F. Powell, Y. Yue, M.J. Renzi, A. Ercan, S. Narayanan, E. Fontes, J. Walther, J. Schaller, S.M. Gruner, J. Wang, X-ray Imaging of Shock Waves Generated by High-Pressure Fuel Sprays, Science, 295 (2002) 1261-1263.

[36] Y.J. Wang, K.S. Im, K. Fezzaa, W.K. Lee, J. Wang, P. Micheli, C. Laub, Quantitative x-ray phase-contrast imaging of air-assisted water sprays with high Weber numbers, Applied physics letters, 89 (2006) 151913.

[37] M. Linne, M. Paciaroni, T. Hall, T. Parker, Ballistic imaging of the near field in a diesel spray, Experiments in fluids, 40 (2006) 836-846.

[38] F. Coletti, M.J. Benson, A.L. Sagues, B.H. Miller, R. Fahrig, J.K. Eaton, Three-Dimensional Mass Fraction Distribution of a Spray Measured by X-Ray Computed Tomography, Journal of Engineering for Gas Turbines and Power, 136 (2014) 051508.

[39] M. Battistoni, C.N. Grimaldi, Numerical analysis of injector flow and spray characteristics from diesel injectors using fossil and biodiesel fuels, Applied Energy, 97 (2012) 656-666.

[40] M. Linne, Imaging in the optically dense regions of a spray: A review of developing techniques, Progress in Energy and Combustion Science, 39 (2013) 403-440.

[41] J. Portillo, S. Collicott, G. Blaisdell, Measurements of axial instability waves in the near exit region of a high speed liquid jet, Physics of Fluids (1994-present), 23 (2011) 124105.

[42] C.H. Bong, Numerical and experimental analysis of diesel spray dynamics including the effects of fuel viscosity, in: Australian Maritime College, University of Tasmania, 2010.

[43] V. Vuorinen, J. Yu, S. Tirunagari, O. Kaario, M. Larmi, C. Duwig, B.J. Boersma, Large-eddy simulation of highly underexpanded transient gas jets, Physics of Fluids (1994-present), 25 (2013) 016101.

[44] J. Shinjo, A. Umemura, Simulation of liquid jet primary breakup: Dynamics of ligament and droplet formation, International Journal of Multiphase Flow, 36 (2010) 513-532.

[45] O. Desjardins, H. Pitsch, Detailed numerical investigation of turbulent atomization of liquid jets, Atomization and Sprays, 20 (2010).

[46] S. Moon, Y. Gao, S. Park, J. Wang, N. Kurimoto, Y. Nishijima, Effect of the number and position of nozzle holes on in-and near-nozzle dynamic characteristics of diesel injection, Fuel, 150 (2015) 112-122.

[47] A.B. Swantek, D. Duke, F.Z. Tilocco, N. Sovis, C.F. Powell, A.L. Kastengren, End of Injection, Mass Expulsion Behaviors in Single Hole Diesel Fuel Injectors, in: ILASS Americas 26th Annual Conference on Liquid Atomization and Spray Systems, Portland, OR, USA, 2014.

[48] S. Moon, Y. Gao, J. Wang, K. Fezzaa, T. Tsujimura, Near-field dynamics of high-speed diesel sprays: Effects of orifice inlet geometry and injection pressure, Fuel, 133 (2014) 299-309.

[49] L. Goldsworthy, N. Ashraf, P. Brandner, Development of a high pressure chamber for research into diesel spray dynamics, Australian Journal of Mechanical Engineering, 7 (2009) 15-34.

[50] E. De Villiers, A.D. Gosman, H.G. Weller, Large eddy simulation of primary diesel spray atomization, SAE transactions, 113 (2004) 193-206.

[51] J.U. Brackbill, D.B. Kothe, C. Zemach, A continuum method for modeling surface tension, Journal of Computational Physics, 100 (1992) 335-354.

[52] O. Ubbink, Numerical prediction of two fluid systems with sharp interfaces, in, University of London PhD Thesis, 1997.

[53] H.G. Weller, A new approach to VOF-based interface capturing methods for incompressible and compressible flow, OpenCFD Ltd., Report TR/HGW/04, (2008).

[54] A. Yoshizawa, K. Horiuti, A statistically-derived subgrid-scale kinetic energy model for the large-eddy simulation of turbulent flows, Journal of the Physical Society of Japan, 54 (1985) 2834-2839.

[55] R.I. Issa, Solution of the implicitly discretised fluid flow equations by operator-splitting, Journal of Computational Physics, 62 (1986) 40-65.

[56] B. Befrui, A. Aye, P. Spiekermann, D.L. Varble, M.A. Shost, M.C. Lai, J. Wang, GDi Skew-Angled Nozzle Flow and Near-Field Spray Analysis using Optical and X-Ray Imaging and VOF-LES Computational Fluid Dynamics, in, SAE Technical Paper, 2013.

[57] H. Jasak, Error analysis and estimation for the finite volume method with applications to fluid flows, (1996).

[58] N. Papadopoulos, P. Aleiferis, Numerical Modelling of the In-Nozzle Flow of a Diesel Injector with Moving Needle during and after the End of a Full Injection Event, SAE International Journal of Engines, 8 (2015) 2285-2302.

[59] M. Battistoni, C. Poggiani, S. Som, Prediction of the Nozzle Flow and Jet Characteristics at Start and End of Injection: Transient Behaviors, SAE International Journal of Engines, 9 (2015).

[60] M. Battistoni, Q. Xue, S. Som, E. Pomraning, Effect of Off-Axis Needle Motion on Internal Nozzle and Near Exit Flow in a Multi-Hole Diesel Injector, SAE International Journal of Fuels and Lubricants, 7 (2014) 167-182.

[61] A. Schmid, B. Von Rotz, R. Schulz, K. Herrmann, G. Weisser, R. Bombach, Influence of nozzle hole eccentricity on spray morphology, in: ILASS 2013, 2013.

[62] F. Salvador, J. Martínez-López, J.-V. Romero, M.-D. Roselló, Study of the influence of the needle eccentricity on the internal flow in diesel injector nozzles by computational fluid dynamics calculations, International Journal of Computer Mathematics, 91 (2014) 24-31.

[63] F. Salvador, J. Martínez-López, M. Caballer, C. De Alfonso, Study of the influence of the needle lift on the internal flow and cavitation phenomenon in diesel injector nozzles by CFD using RANS methods, Energy conversion and management, 66 (2013) 246-256.

[64] R. Marcer, C. Audiffren, B. Yerly, Influence of the needle lift motion on cavitating flow inside Diesel injector, in: 12th Triennial International Conference on Liquid Atomization and Spray Systems, ILASS Heidelberg, Germany, 2012, pp. 2-6.

[65] M. Ghiji, L. Goldsworthy, P.A. Brandner, V. Garaniya, P. Hield, Numerical and experimental investigation of early stage diesel sprays, Fuel, 175 (2016) 274–286.

[66] J. Shinjo, A. Umemura, Detailed simulation of primary atomization mechanisms in Diesel jet sprays (isolated identification of liquid jet tip effects), Proceedings of the Combustion Institute, 33 (2011) 2089-2097.

[67] H. Jasak, H.G. Weller, A.D. Gosman, High resolution NVD differencing scheme for arbitrarily unstructured meshes, International journal for numerical methods in fluids, 31 (1999) 431-449.

[68] S. B. Pope, Turbulent Flows, Measurement Science and Technology, 12 (2001).

[69] R. Payri, F. Salvador, J. Gimeno, J. De la Morena, Macroscopic behavior of diesel sprays in the near-nozzle field, in, SAE Technical Paper, 2008.

[70] J.V. Pastor, J.J. López, J.M. García, J.M. Pastor, A 1D model for the description of mixing-controlled inert diesel sprays, Fuel, 87 (2008) 2871-2885.

[71] R. Klein-Douwel, P. Frijters, L. Somers, W. De Boer, R. Baert, Macroscopic diesel fuel spray shadowgraphy using high speed digital imaging in a high pressure cell, Fuel, 86 (2007) 1994-2007.

[72] J. Shinjo, A. Umemura, Surface instability and primary atomization characteristics of straight liquid jet sprays, International Journal of Multiphase Flow, 37 (2011) 1294-1304.

[73] N. Dumont, O. Simonin, C. Habchi, Cavitating flow in diesel injectors and atomization: a bibliographical review, in: 8th International Conference on Liquid Atomisation and Spray Systems, Pasedena, CA, 2000.

[74] J.M. Desantes, J. Pastor, A. Doudou, Study of the steady flow produced by direct injection diesel engine intake ports, Proceedings of the Institution of Mechanical Engineers, Part D: Journal of Automobile Engineering, 215 (2001) 285-298.

[75] J. Benajes, J. Pastor, R. Payri, A. Plazas, Analysis of the influence of diesel nozzle geometry in the injection rate characteristic, Journal of fluids engineering, 126 (2004) 63-71.

[76] H.W. Liepmann, A. Roshko, Elements of gasdynamics, Courier Corporation, 1957.